Oncometabolism Drives Autophagy Activation in Skeletal Muscle

Anja Karlstaedt[1*], Heidi Vitrac[2], Rebecca L. Salazar[1], Benjamin D. Gould[1], Daniel Soedkamp[3], Weston Spivia[3], Koen Raedschelders[3], An Q. Dinh[4], Anna Guzman[5], Lin Tan[6], Stavros Azinas[2], David Taylor[7], Walter Schiffer[8], Daniel McNavish[9], Helen B. Burks[1], Roberta A. Gottlieb[7], Philip L. Lorenzi[6], Blake M. Hanson[4], Jennifer E. Van Eyk[3], Heinrich Taegtmeyer[1]

[1] Department of Internal Medicine, Division of Cardiology, McGovern Medical School at The University of Texas Health Science Center at Houston, Houston, TX 77030, USA

[2] Department of Biochemistry, McGovern Medical School at The University of Texas Health Science Center at Houston, Houston, TX 77030, USA

[3] Advanced Clinical Biosystems Research Institute, The Smidt Heart Institute, Cedars-Sinai Medical Center, Los Angeles, CA 90048, USA

[4] Center for Infectious Diseases, School of Health, The University of Texas Health Science Center at Houston, Houston, TX 77030, USA

[5] Center for Stem Cell and Regeneration, Baylor College of Medicine, Houston, TX, 77030, USA

[6] Department of Bioinformatics and Computational Biology, The University of Texas MD Anderson Cancer Center, Houston, TX, 77054, USA

[7] The Smidt Heart Institute, Cedars-Sinai Medical Center, Los Angeles, CA 90048, USA

[8] Department of Internal Medicine, Washington University School of Medicine in St. Louis, St. Louis, MO, 63110, USA

[9] Department of Internal Medicine, Wake Forest School of Medicine, Winston-Salem, NC, 27101, USA

[*] Corresponding Author and Lead Contact: A.K. (Anja.Karlstaedt@uth.tmc.edu)

SUMMARY

Metabolic rewiring is a well-established feature of muscle cells and a hallmark of cancer. In isocitrate dehydrogenase 1 and 2 mutant tumors, increased production of the oncometabolite D-2-hydroxyglutarate (D2-HG) is associated with myopathy. The connection between metabolic changes and proteomic remodeling in skeletal muscle remains poorly understood. We demonstrate that D2-HG impairs NAD^+ redox homeostasis in myocytes, causing activation of autophagy via de-acetylation of microtubule-associated protein 1 light chain 3-II (LC3-II) by the nuclear deacetylase Sirt1. We integrated multi-omics data from mice treated with D2-HG and demonstrate that autophagy activation leads to skeletal muscle atrophy and sex-dependent metabolic and proteomic remodeling. We also characterized protein and metabolite interactions linking energy-substrate metabolism with chromatin organization and autophagy regulation. Collectively, our multi-omics approach exposes mechanisms by which the oncometabolite D2-HG induces metabolic and proteomic remodeling in skeletal muscle, and provides a conceptual framework for identifying potential therapeutic targets in cachexia.

INTRODUCTION

Skeletal muscle wasting is a hallmark of cachexia, which is associated with systemic multi-organ diseases like heart failure and cancer (Evans et al., 2008; Fearon et al., 2011). Patients with cachexia have a poor prognosis in advanced disease stages, and about 20 to 30% of cancer-associated deaths are due to cachexia (Fearon et al., 2011). The severity of skeletal muscle atrophy can be associated with specific tumor type rather than with tumor size and burden (Fearon et al., 2011). Severe muscle loss is commonly associated with hematological malignancies (e.g., leukemia), pancreatic tumors, non-small cell lung tumors, and gastrointestinal tract tumors (Lok, 2015). The genetic and metabolic basis for the development of skeletal muscle atrophy is elusive and limits our ability to develop targeted therapeutic strategies without those side effects.

Recent studies indicate that skeletal muscle atrophy during cachexia is characterized by increased proteome proteolysis (Gallagher et al., 2012; Salazar-Degracia et al., 2019), impaired mitochondrial metabolism (Friesen et al., 2015), inefficient ATP provision (VanderVeen et al., 2017), dysfunction of the electron transport chain (VanderVeen et al., 2017), and extensive cellular lipid remodeling (Kir and Spiegelman, 2016). Those molecular changes are not just a severe complication of tumor growth, but rather a consequence of the metabolic reprogramming driven by the biology of tumors (Gallagher et al., 2012). The metabolic phenotype of tumors is often characterized by the accumulation of specific intermediates or oncometabolites.

We previously reported that the oncometabolite D-2-hydroxyglutarate (D2-HG) promotes contractile dysfunction in the heart (Karlstaedt et al., 2016). Mutations of isocitrate dehydrogenase (IDH) 1 and 2 lead to the gain of a neo-morphic enzymatic function and production of the oncometabolite D2-HG, which accumulates to millimolar level in both tumors and the bloodstream (DiNardo et al., 2013; Kranendijk et al., 2010a; Kranendijk et al., 2012; Kranendijk et al., 2010b). IDH 1 and 2 mutations are observed in several types of cancers including glioblastomas (Louis et al., 2016; Miller et al., 2019), acute myeloid leukemia (AML) (Cancer Genome Atlas Research et al., 2013), chondrosarcoma (Lu et al., 2013), and cholangiocarcinoma (Amary et al., 2011; Pansuriya et al., 2011). Our previous studies showed that the oncometabolite D2-HG suppresses energy-provision, decreases α-KG levels and impairs NADH regeneration in the heart through inhibition of α-ketoglutarate dehydrogenase (α-KGDH) (Karlstaedt et al., 2016). Prolonged exposure to D2-HG was associated with both heart

and skeletal muscle atrophy in mice, which prompted the hypothesis that oncometabolic stress mediates autophagy or proteasomal degradation of muscle proteins.

Protein synthesis and breakdown in skeletal muscle is regulated by a variety of factors, including nutrient supply, hormone concentrations, and physical activity. Muscle mass homeostasis is maintained through balancing rates of protein synthesis and degradation, the latter including the ubiquitin/proteasome pathway (UPP), autophagy, caspases, cathepsins, and calcium-dependent calpains. Previous studies have demonstrated the involvement of the UPP with increased mRNA expression of muscle-specific E3 ubiquitin ligases, including atrogin-1 or maf box 1 (MafBx1) and muscle-specific ring finger protein 1 (Murf1 or Trim63), during the acute stress response in skeletal muscle (Bodine et al., 2001; Gomes et al., 2001). Several studies have implicated both protein synthesis and degradation pathways in animal models of cancer-associated muscle wasting (Gallagher et al., 2012; Smith and Tisdale, 1993). Similarly, increased α-KG metabolism prevents activation of autophagy (Baracco et al., 2019).

Our goal was to characterize the metabolic, proteomic, and genomic changes in skeletal muscle that occur in response to D2-HG and understand which biological processes are involved in driving adaptation. We devised a multi-omics approach to study the system-wide impact of D2-HG on skeletal muscle metabolism and physiology in cell culture and mouse models. We link gene and protein expression to metabolic changes and reveal the complex interplay between biological processes in response to acute and chronic stress. We show that the NAD-dependent sirtuin 1 signaling pathway integrates protein and nutrient signals to regulate autophagy in response to oncometabolic stress. Targeted metabolomics revealed that changes in autophagy activation affect the metabolism of energy-providing substrates in skeletal muscle cells. Importantly, using an integrative multi-omics approach, we show that these changes induce a system-wide adaptive response in mouse models that affect both gene and protein expression profiles. This study highlights the importance of system-wide profiling to decipher complex biological adaptation in response to oncometabolic stress and provides an integrated approach to modeling cancer cachexia in the context of IDH-mutant cancers.

RESULTS

Inhibition of α-KGDH causes metabolic remodeling in skeletal muscle cells.

To explore the metabolic changes in skeletal muscle cells in response to D2-HG, we assessed metabolism directly *in vitro* through functional assays and metabolomics. Because D2-HG has a similar molecular structure as α-KG, it can inhibit α-KG-dependent enzymes, including α-KGDH, leading to decreased Krebs cycle flux (Karlstaedt et al., 2016). We hypothesized that mitochondrial α-KG metabolism regulates metabolic adaptation in response to oncometabolic stress in skeletal muscle. L6 myocytes (rat skeletal muscle cell line) were differentiated into myotubes (L6Ms) over 72 h and treated with or without D2-HG (1 mmol/L) for 24 h in defined nutrient-rich media (**Figure 1A**). Myotubes consists of fused myoblasts, which retrain the ability to contract (Oberg et al., 2011).

We first determined the effect of D2-HG (ranging from 0.06 to 1.0 mmol/L) on mitochondrial function in differentiated L6 myotubes using Agilent Seahorse XF Cell Mito Stress Tests. D2-HG decreases the ATP-linked oxygen consumption rate (OCR) and increases the mitochondrial spare capacity in L6 myotubes in a concentration-dependent manner (**Figure 1B** and **S1A**). Intriguingly, we did not observe decreased mitochondrial function or changes in ATP-related OCR at D2-HG concentration between 0.06 and 0.125 mmol/L (**Figure S1A** and **S1B**). Those observations are consistent with previous reports that D2-HG or L2-HG may accumulate under physiologic conditions without a notable effect on enzymatic activities in certain cancer cell lines and tumors (Intlekofer et al., 2015; Intlekofer et al., 2017; Nadtochiy et al., 2015). A key step of anaplerosis is the incorporation of α-KG into the Krebs cycle. Therefore, we compared the effect of D2-HG to dimethyl alpha-ketoglutarate (DMKG, 1.0 mmol/L), a membrane-permeable ester of α-KG that is cleaved to α-KG in the cytoplasm and, consequently, increases α-KG levels (Shah et al., 2010). In cultured differentiated L6 myotubes, DMKG (1.0 mmol/L) decreased ATP provision and increased mitochondrial spare capacity (**Figure 1B**). Those mitochondrial respiration changes in DMKG-treated L6Ms were comparable to cells treated with 0.5 to 1.0 mmol/L D2-HG (**Figure 1B**).

Metabolic changes were assessed using targeted liquid chromatography and mass spectrometry (LC-MS/MS) in differentiated L6Ms that were treated with or without D2-HG (1.0 mmol/L) or DMKG (1.0 mmol/L) (see Methods for details). The principal component analysis

revealed a clear separation between treatment and control groups (**Figure 1C**), indicating that both D2-HG and DMKG treatment promoted considerable metabolic remodeling in L6Ms. Unsupervised hierarchical clustering of the metabolic profiles revealed that both D2-HG and DMKG decreased the availability of critical intermediates in glycolysis (glucose 6-phosphate, fructose 6-phosphate) and pentose phosphate pathway (sedoheptulose-1,7-bisphosphatase and 6-phosphogluconic acid). Simultaneously, D2-HG treatment increased amino acids (e.g., glutamate,), α-KG and NAD^+, whereas treatment with DMKG did not affect these metabolites (**Figure 1D**). Our analysis shows that D2-HG treatment increases succinate, isocitrate, and NAD^+ levels in skeletal myotubes. These findings suggest that inhibition of α-KGDH by D2-HG impacts the NAD^+/NADH redox potential, similar to our previous findings in tissue from rodent hearts (Karlstaedt et al., 2016).

Next, we integrated the targeted LC-MS/MS metabolomic data into pathway enrichment analysis to assess metabolic remodeling based on pathways and chemical similarity using MetaMapp (Barupal et al., 2012) (**Figure 1E**). The reconstructed network was visualized using Cytoscape (Shannon et al., 2003). The resulting network is composed of 101 metabolites with 615 metabolite-metabolite interactions (MMIs). Our analysis revealed that D2-HG increases amino acid and glucose metabolism, the pentose phosphate pathway (PPP), and redox homeostasis in cultured differentiated L6Ms. We next tested whether D2-HG-mediated mitochondrial function changes are driven by glutamine or α-KG metabolism. We measured α-KG concentration in L6Ms in the presence or absence of the glutamate synthase inhibitor, bis2-(5phenylacetamido-1,3,4,-thiadiazol-2-yl)ethyl-sulfide),(2-bromoethyl) trimethylammonium bromide (BPTES, 20 μmol/L), DMKG (1.0 mmol/L) or D2-HG (1.0 mmol/L) after 24 h treatments. Both D2-HG and BPTES caused a decrease of α-KG levels, whereas DMKG increased α-KG in our experimental conditions (**Figure 1C and S1C**). Those findings suggest that α-KG is a critical downstream effector of D2-HG in skeletal muscle cells. A moderately high level of D2-HG causes mitochondrial dysfunction in L6Ms, which parallels broad metabolic remodeling through increased amino acid metabolism and demand for glutamine.

Inhibition of α-KGDH by D2-HG Increases Autophagic Flux in L6Ms

Recent studies indicate that disruption of α-KG metabolism and NAD^+ redox homeostasis regulates and induces autophagic flux (Baracco et al., 2019; Marino et al., 2014b). To assess

whether D2-HG also mediates the activation of autophagy, we analyzed the flux of autophagosome formation in differentiated L6Ms cultured in defined nutrient-rich media and treated with or without D2-HG (0.5 and 1.0 mmol/L). To assess the initiation of autophagosome formation, we quantified the expression of microtubule-associated protein 1 light chain 3-II (LC3-II) using western blotting. Autophagy is a dynamic process. The formation of autophagosomes is balanced by the turnover and delivery to lysosomes. Therefore, bafilomycin A1 (BafA1), a selective vacuolar H^+ ATPase (V-ATPase) inhibitor, was used to measure autophagic flux. BafA1 inhibits the maturation of autophagosomes by blocking the fusion between autophagosomes and lysosomes, thus preventing LC3-II degradation (Klionsky et al., 2016; Yamamoto et al., 1998). We found that D2-HG increases the lipidation of LC3 with and without bafilomycin A1 (BafA1, 200 nmol/L) (**Figure 2A** and **B**). In contrast, the supplementation of DMKG maintained low autophagy levels (LC3-II and p62 expression) both with and without BafA1 conditions *in vitro* (**Figure S2A** and **S2B**). Similarly, the number of autophagic puncta per cell were measured through live-cell fluorescent microscopy in L6Ms expressing green fluorescent protein (GFP) fused with LC3 (see Methods for details). The fusion between autophagosomes and lysosomes can be visualized using LC3 and LysoTracker (see **Methods** for details) as markers for autophagosomes and lysosomes. In untreated L6Ms (phosphate-buffered saline, PBS; control), GFP-LC3 puncta were diffusely localized in the nucleus and cytosol (**Figure 2C** and **D**). As expected, BafA1 treatment caused a significant increase in GFP-LC3 puncta formation in the cytosol and autolysosome formation in L6Ms incubated in defined growth media without D2-HG, reflecting the basal level of autophagy activation (**Figure 2C** and **D**). In contrast, GFP-tagged LC3 in L6Ms treated with D2-HG (1 mmol/L) resided primarily in the cytoplasm with multiple cytoplasmic puncta. The majority of GFP-LC3 colocalized with LysoTracker consistent with increased autophagic flux (**Figure 2C** and **D**). We also measured the expression of critical genes involved in autophagy: Beclin1, LC3, MafBx1, Murf1, and protein 62 (p62) were measured over 24 hrs. Gene expression of both LC3 and Murf1 increased within 12 h of treatment *in vitro*, reaching a plateau after 16 h and staying significantly increased at 24 h (**Figure 2E** and **F**). In contrast, MafBx1 mRNA levels remained unchanged between experimental groups during the 24 h experimental protocol (**Figure S2C**). Beclin1 mRNA levels increased after 2 h in D2-HG-treated cells (**Figure S2D**), while p62 expression decreased after 8 h before returning to the

baseline level (**Figure S2E**). These results demonstrate that D2-HG increases autophagic flux in skeletal muscle cells.

Deacetylation of LC3 is driven by Sirt1 activation

Next, we wanted to elucidate how D2-HG mediates LC3 redistribution into the cytosol and its subsequent lipidation. Seahorse experiments indicated that D2-HG (1.0 mmol/L) decreases ATP provision in cultured differentiated L6Ms after 24 h. One mechanism could involve the AMP-activated protein kinase (AMPK) and the mammalian target of rapamycin (mTOR) which are crucial cellular energy sensor proteins regulated by ATP levels in the cell. Therefore, we assessed the activation of AMPK and mTOR by measuring the extent of their phosphorylation status using western blotting. The total and phosphorylated protein expression of AMPK and mTOR were not statistically significantly increased after treatment with D2-HG (*P*-value>0.05 for all groups; **Figure S3A**). The addition of BafA1 (20 nmol/L; for 2 h) also showed no statistical significance between control and treatment groups (*P*-value>0.05 for all groups; **Figure S3B**).

A second possible mechanism could revolve around NAD-dependent deacetylase sirtuin-1 (Sirt1) as previous studies have shown that during starvation, the Sirt1 can activate autophagy through de-acetylation of LC3 lysine residues at position 49 and 51 (**Figure 3A**) (Huang et al., 2015). In this model, D2-HG increases the co-localization of LC3 and Sirt1, which, in turn, decreases the acetylation of LC3 in differentiated L6Ms (**Figure 3B**). To further explore this, we developed single and double mutants of LC3 with replacement of lysine at positions 49 and 51 by either arginine (LC3-K49R, LC3-K51R and LC3-K49R-K51R) or glutamine (LC3-K49Q, LC3-K51Q and LC3-K49Q-K51Q). These mutations allowed to mimic a decrease (K to R) or an increase (K to Q) in the acetylation level of LC3 (Huang et al., 2015). GFP-tagged single and double mutants were transfected into L6Ms and further differentiated into myotubes to assess their acetylation after treatment with or without D2-HG (1.0 mmol/L) for 24 h. Lysine-to-arginine single replacement at position 49 or 51 reduced LC3 acetylation, and the double mutant (LC3-K49R-K51R) showed the lowest acetylation (**Figure 3C**). Upon treatment with D2-HG, we detected increased deacetylation of LC3 in L6Ms expressing LC3-K49R or LC3-K51R. LC3 acetylation was almost completely abolished in LC3-K49R-K51R mutants and associated with increased LC3 lipidation (**Figure 3C**). Conversely, we found increased acetylation of LC3 in

L6Ms expressing GFP-tagged LC3-K to Q mutants treated with and without D2-HG (**Figure S3C** and **S3D**). In all mutants, LC3 acetylation was decreased in D2-HG cells compared to untreated cells, indicating that the oncometabolite D2-HG increases the flux of deacetylation *in vitro* (**Figure S3D**). We then measured the formation of GFP-LC3 containing puncta in GFP-tagged LC3-KR mutants through live-cell fluorescent microscopy. Untreated L6Ms expressing LC3-K48R, LC3-K51R or LC3-K48R-K51R showed a nuclear and cytoplasmic distribution like wild type (WT) LC3, which was also reflected in the amount of GFP-LC3 containing puncta per cell (**Figure 3D**). In contrast, treatment with D2-HG caused 2 to 3 -fold increased formation of GFP-LC3 puncta in the cytosol (**Figure 3D**). Our findings indicate that the deacetylation of LC3 is the primary driver of autophagy activation in D2-HG treated L6Ms.

Next, we tested whether the activation of autophagy is attenuated by increasing the deacetylation of LC3. We used two strategies to test this hypothesis. First, we silenced the expression of Sirt1 using siRNA and non-targeting negative controls to assess whether Sirt1 is solely driving the lipidation of LC3. Secondly, we transfected L6Ms with a plasmid that resulted in the overexpression of the acetyltransferase p300 to test whether increased protein acetylation would counteract the effect of D2-HG. Previous studies have shown that p300 is a primary regulator of autophagy through protein acetylation during nutrient limitation (Lee and Finkel, 2009). At baseline, protein expression of both Sirt1 and p300 were increased in response to D2-HG (**Figure 3E**). Silencing Sirt1 (**Figure 3F**) attenuated both the total LC3-II level and the LC3-II to LC3-I ratio compared to WT conditions within 24 h (**Figure 2A**). Nonetheless, both total LC3-II level (*P*-value = 0.0004; q-value = 0.0008) and LC3-II to LC3-I ratio (P-value = 0.02; q-value = 0.023) were still significantly increased compared to WT conditions. These data suggest that other sirtuin isoforms may contribute to autophagy activation in the presence of D2-HG. In contrast, overexpressing p300 (**Figure 3G**) fully attenuated total LC3-II levels (*P*-value = 0.5; q-value = 0.7) and LC3-II to LC3-I ratios (*P*-value = 0.6; q-value = 0.7) within 24 h, thus counteracting the effect of D2-HG. Our data indicate that NAD^+ redox changes and the deacetylation of LC3 drive autophagy in response to D2-HG treatment *in vitro*.

In vivo **effect of autophagy activation in response to D2HG**

Taken together our data demonstrate that oncometabolic stress induces extensive metabolic remodeling in the L6Ms and induces autophagy activation through increased deacetylation of

LC3 via Sirt1. To probe the biological importance and long-term consequences of D2-HG-mediated remodeling in skeletal muscle, wild type (WT) male and female mice (four animals per group; 10 weeks old) were treated for 30-days with either vehicle (PBS) or D2-HG (450 mg/kg body weight) through daily intraperitoneal injections (IP) (**Figure S4A)**. We observed increased body weight in both males and females, which directly correlated with the overall growth of the animals (**Figure S4B**). As expected, we observed a reduction in *M. gastrocnemius* weight (both left and right muscles) in male animals with D2-HG compared to placebo treatment after 30 days of treatment (**Figure S4C**). Correspondingly, we found increased D2-HG levels in muscle tissue from male animals (**Figure S4D**). In contrast, both *M. gastrocnemius* weight and D2-HG levels were unchanged in female mice (**Figure S4C** and **S4D**).

To assess the functionality of mice skeletal muscle, grip strength was determined in mice by conducting a series of weekly *in vivo* weight-lifting tests during the 30-day treatment protocol (Contet et al., 2001; Deacon, 2013). Mice lifted weights ranging from 20 to 90 g for a maximum of 3 seconds (**Figure 4A**). For each weight a mouse was able to lift successfully, the animal received a point based on a score-table (see **Methods** for details). In untreated control animals (male and female), grip strength increased in correlation with the animals' overall growth (**Figure 4B**). Importantly, this growth-dependent increase in grip strength was absent in both males and females when treated with D2-HG (**Figure 4B**). After four weeks of treatment with D2-HG, the grip strength was significantly reduced in both male and female animals (male, *P*-value = 0.019; female, *P*-value = 0.0207). Histological analysis of *M. gastrocnemius* sample (**Figure 4C**) revealed that the reduction in muscle mass in D2-HG treated male mice was caused by a reduction in the myofiber nuclei number (**Figure 4D**). The LC3-II expression in *M. gastrocnemius* samples from male animals was reduced in D2-HG treated animals. Total LC3 levels were almost depleted (**Figure 4E**), with an accompanying 20-fold increase in p62 expression in skeletal muscle (**Figure 4E**). These findings show that prolonged treatment with D2-HG promotes disruption of LC3-mediated autophagy and p62 aggregation.

Transcriptional and post-transcriptional regulation of oncometabolic stress

To investigate the profile and extent of transcriptional, post-transcriptional, and metabolic events upon oncometabolic stress by D2-HG, our animal studies were complemented by applying an integrated systems biology-wide approach (**Figure S5A**). Male and female mice were treated

for 30-days with vehicle (PBS) or D2-HG (450 mg/kg body weight) through daily IP (four animals per group). In-depth multi-omics profiling was conducted on each skeletal muscle tissue sample (*M. gastrocnemius*) with RNA sequencing (RNA-seq; transcriptomics) and LC-MS/MS for proteomics and targeted metabolomics (n = 8; 4 x PBS, 4 x D2-HG). Proteins were sub-fractionated into the highly abundant myofilamentous proteins, cytosolic proteins, and insoluble membrane proteins (Kane et al., 2007) prior to analysis by LC-MS/MS for identification and relative quantification (see **Methods** for details). We identified a total of 46,079 transcripts using RNA-Seq, quantified 2,153 proteins from untargeted analysis using LC-MS/MS, and quantified 95 metabolites from targeted analysis using LC-MS/MS. PCA analysis of protein and gene expression data showed a clear separation between treatment and control groups (**Figure 5A**). In total, we identified 1,976 differentially expressed genes (FDR < 1%, **Figure S5B**) and 170 differentially expressed proteins (FDR < 5%, **Figure S5B**). Unsupervised hierarchical cluster analysis showed a clear separation between treatment groups and sex (**Figure S5C**). Similarly, unsupervised hierarchical clustering of significantly regulated proteins revealed four main clusters (**Figure S6D**). We identified 21 enriched pathways (Gene ontology processes) using the Search Tool for the Retrieval of Interacting Genes/Proteins database (STRING, FDR < 0.01; **Figure 5B**) (Szklarczyk et al., 2019), and the 'ATP metabolic process' pathway was ranked first. Functional enrichment analysis showed that proteins in these clusters are part of cellular protein metabolic processes, regulation of chromatin assembly or disassembly, mitochondrial ATP provision, and muscle contraction (**Figure 5B**). Next, we reconstructed a protein-protein interaction (PPI) network of significantly regulated proteins using STRING (Szklarczyk et al., 2019). The network consists of 70 proteins (nodes) and 170 protein-protein interactions (edges) (**Figure 5C**). This analysis revealed that the PPI network of skeletal muscle was divided into four main clusters: (1) mitochondrial respiratory chain complex assembly, (2) cell protein metabolic process, (3) cellular processes, and (4) chromatin assembly and disassembly.

Normalized counts from RNA-seq could be matched with protein MS intensities for 1,346 genes independent of sex. Plotting individual RNA and protein ratios (D2-HG vs. PBS) revealed several proteins with differential expression at both the transcript and protein level (**Figure S6A**). RNA and protein abundance ratios correlated only poorly (Pearson's correlation coefficient, r = 8.9), indicating translational, miRNA or post-transcriptional regulation of many biological processes in response to oncometabolic stress in skeletal muscle. Intriguingly, several proteins

that are part of autophagy regulation, lipid remodeling and known regulators of mitochondrial function, including the NADH dehydrogenase 1 alpha subcomplex subunit 13 (encoded by Ndufa 13), the quinone oxidoreductase (encoded by Cryz) and D-beta-hydroxybutyrate dehydrogenase (encoded by Bdh1), were only regulated at the protein level (**Figure S6A**). Further, we identified specific genes and proteins with differential regulation that are part of chromatin organization and acetylation (Chd1 and histone 1.2), structural remodeling (dynein), and autophagy regulation (Sirt 2, Lamp1 and Bag3). Both Chd1 and Histone 1.2 (**Figure 5D**) showed increased protein expression in male and female mice treated with D2-HG, while gene expression was decreased. In contrast, the expression of the lysosome-associated membrane glycoprotein 1 (Lamp1) and Bag 3 (a co-chaperone for HSP70 and HSC70) was only upregulated at the protein level in D2-HG-treated male and female mice (**Figure 5E**), respectively. The gene and protein expression of Sirt2 and dynein were decreased for both male and female mice in treatment groups (**Figure 5F**). Together these findings elucidate the adaptation to D2-HG treatment *in vivo* through the remodeling of chromatin to active, targeted gene programs, followed by protein expression. To compare the proteomic and transcriptomic datasets in terms of gene categories, we used a 2D annotation enrichment algorithm (Cox and Mann, 2012). This algorithm identifies both correlated and uncorrelated changes between two data dimensions. Our analysis revealed different strategies in males and females to compensate for the metabolic stress caused by the oncometabolite D2-HG (**Figure S6B** and **S6C**). Overall, male animals showed a reduction in proteins that are part of oxidative phosphorylation, whereas female animals upregulated the same set of proteins. Our data clearly show that proteomic remodeling in response to oncometabolis stress is very different between male and female mice. Our analysis is a first step for the investigation of sex-dependent mechanisms in cachexia and oncometabolic stress, for instance, based on the enrichment for metabolic proteins.

Metabolomic signatures and multi-omics data integration

There is notable metabolite rewiring that are D2-HG-dependent and gender-dependent (**Figure 6A**). Principal component analysis showed that D2-HG treatment promoted broad metabolic changes in male animals, whereas D2-HG had only a limited effect on female animals (**Figure 6A**). The metabolic profile in males showed broad changes in carbohydrate and amino acid

metabolism (**Figure 6B** and **Figure S7A**). Specifically, we found an increased relative abundance of pyruvate, lactate, erythrose 4-phosphate, α-KG, succinate, and amino acids (leucine, lysine and methionine) in male mice treated with D2-HG. In contrast, the abundance of fumarate, malate, and adenylsuccinate decreased in both sexes in response to D2-HG treatment (**Figure 6B**). We used MetaMapp (Barupal et al., 2012) to integrate information from targeted MS-based metabolomics and to visualize the metabolic profile in response to D2-HG using cytoscape (Shannon et al., 2003) (**Figure 6C**). Unsupervised hierarchical clustering of targeted metabolomics revealed four main clusters comprising 15 metabolic pathways using the Reactome pathway knowledgebase (Jassal et al., 2020) (**Figure S7B**). Broadly, metabolites were enriched in pathways that are part of the pyrimidine metabolism, nucleotide metabolism, energy substrate metabolism, and DNA replication.

Next, we used the set of metabolites from targeted metabolomics to identify the directly interacting proteins (e.g., metabolic enzymes) using the Reactome pathway knowledgebase (Jassal et al., 2020). In total we identified 361 identified protein-metabolite interactions (PMIs). The correlation between changes in metabolite level and protein expression was determined using both Spearman's rank and Pearson correlation coefficient. Both statistical measures showed a very good overlap (**Figure S6C**). We integrated 25 metabolites and 49 proteins into a network using a Spearman's rank and Pearson correlation coefficient cut-off value of 0.75. The metabolic network is composed of 60 PMIs, 76 MMIs, and 229 PPIs (**Figure 6D**). We identified four main clusters of interactions that encompassed the (1) pyrimidine/co-factor metabolism, (2) amino acid metabolism, (3) Krebs cycle (or tricarboxylic acid cycle), as well as (4) glycolysis and the pentose phosphate pathway. Several core proteins interacted with multiple metabolites and PMIs preferentially occurred within a metabolic sub-network. For example, PMIs identified for glycolysis intermediates were both enriched in proteins for "glycolysis/pentose phosphate pathway," and glucose-binging proteins were also enriched for the glycolysis (P-value<0.001). Our analysis shows the combined regulation of metabolic function through up- or down-regulation of proteins that are part of metabolic pathways and corresponding metabolite levels. For example, the upregulation of betaine-homocysteine S-methyltransferase (Bhmt) and branched-chain keto acid dehydrogenase E1 subunit beta (Bckdhb) expression correlated with an increased level of aspartate and methionine. Further, we identified five up-regulated proteins, Dnm1l, Rab10, Rac1, Cdc42 and Eif2s3x, that are part of cell signaling, organelle and

microtubule organization, as well as myoblast fusion in mice and that are often co-expressed (Barabutis et al., 2018; Moore et al., 2019; Sylow et al., 2013; Vasyutina et al., 2009). The actin cytoskeleton-regulating GTPase, Rac1, is a known regulator of actin remodeling and contraction-induced glucose uptake through GLUT4 translocation. Correspondingly, we observed increased levels of AMP and glycolytic intermediates (e.g., glucose, fructose 6-phosphate), as well as an upregulation of proteins involved in glycolysis and the pentose phosphate pathway. These findings suggest that many core metabolic proteins response to D2-HG-mediated metabolic signals. Our multi-omics analysis further demonstrated the close interaction between protein and metabolite profiles in response to oncometabolic stress.

DISCUSSION

Our study revealed that the oncometabolite D2-HG promotes autophagy activation in skeletal muscle, and broad proteomic and metabolomic remodeling independent of sex. The response to oncometabolic stress includes early (e.g., energy substrate metabolism, altered redox state, and autophagy activation) and late events (e.g., structural protein remodeling, protein quality control, and chromatin remodeling) (**Figure 6E**). The combination of *in vitro* and *in vivo* multi-omics studies provided a comprehensive insight into the link between metabolic alteration and protein response pathways. We demonstrated that D2-HG impairs mitochondrial function in L6Ms, which increases NAD^+ levels and activation of LC3-II, a key regulator of autophagy, through deacetylation by the nuclear deacetylase Sirt1. Consequently, increased expression of the protein acetylase p300 or decreased expression of Sirt1 prevented the activation of autophagy. In a mouse model of chronic D2-HG exposure, we also found that oncometabolic stress causes muscle atrophy, decreased grip strength, and increased expression of autophagy markers. Finally, a multi-omics analysis of transcriptomic, proteomics and metabolic data revealed a systems-wide remodeling in skeletal muscle in response to oncometabolic stress.

Several lines of evidence indicate that D2-HG directly mediates autophagy and skeletal muscle atrophy. As there is no single autophagy marker, we used a series of experiments to answer whether D2-HG activates autophagy using cultured differentiated L6Ms. Gene expression shows a time-dependent activation of autophagy after treatment with D2-HG. Previous studies showed that LC3-II formation precedes an increased p62 expression during

the activation of autophagy (Gonzalez-Rodriguez et al., 2014; Pan et al., 2020; Runwal et al., 2019). Our experiments indicate that within 2 h after D2-HG treatment, Beclin1 expression increases rapidly, followed by a decreased p62 expression after 8 h. Correspondingly, we observed an increased LC3 expression within 12 h that was associated with increased Murf1 expression. Together these findings support the conclusion that D2-HG activates autophagy rapidly upon cellular exposure. These findings were corroborated in live-cell imaging using GFP-tagged LC3. Murf1 is an E3 ubiquitin ligase that mediates the ubiquitination and subsequent proteasomal degradation of muscle proteins (e.g., cardiac troponin I/TNNI3) and other sarcomere-associated proteins. Its role in muscle atrophy and hypertrophy is through regulating an anti-hypertrophic PKC-mediated signaling pathway (Arya et al., 2004).

When using targeted metabolomics and functional mitochondria functional assays, we found that D2-HG impaired mitochondrial ATP provision and increased the NAD^+ redox state. These findings agree with our previous studies in isolated working rat hearts, showing that D2-HG inhibits alpha-KGDH (Karlstaedt et al., 2016). Using mutant LC3, we confirmed that autophagy activation in response to D2-HG is mediated through the deacetylation of LC3 by the nuclear deacetylase Sirt1. These findings are consistent with several recent reports that nuclear deacetylation of LC3 is driving autophagy during cell stress (e.g., starvation) (Huang et al., 2015; Marino et al., 2014a; Shen et al., 2020; Yi et al., 2012; Zhao et al., 2016). Acetylation has emerged as an important post-translational modification that affects every step within the autophagic cascade. During periods of nutrient deficiency, cells initiate autophagy to replenish substrates for macromolecular synthesis. Our findings provide additional evidence that Sirt1 drives the deacetylation of LC3 in the absence of nutrient deprivation. Cell starvation evokes several cellular signaling pathways, including activation of AMPK and inactivation of mTOR. We did not observe an increased activation of AMPK in our *in vitro* experiments. The silencing of Sirt1 was sufficient to decrease autophagy, and p300 overexpression attenuated autophagy. Together our data suggest that LC3-dependent mechanisms primarily drive autophagy activation in response to D2-HG.

Our studies indicate that α-KG metabolism is driving the protein acetylation changes within the autophagic cascade. Mechanistic challenges arise from linking metabolic changes to corresponding protein post-translational modifications and whether they are direct or indirect

effects induced by metabolites. The argument supporting our conclusions that autophagy is mediated directly through metabolic changes in the presence of D2-HG is the timing and concentration-dependent effects. As discussed above, metabolic alterations and acetylation of LC3 are sensitive to cellular α-KG levels and mitochondrial function. When D2-HG is elevated to 0.125 mM in L6Ms mitochondrial respiratory capacity is impaired, and both LC3 gene expression and lipidation increase within 12 h. Overexpression of p300 reverses the LC3 lipidation to control levels. Together these findings provide strong evidence that the observed effects are directly mediated through metabolic changes.

Using a multi-omics analysis of skeletal muscle from mice treated for one month with D2-HG, we identified a sex-specific metabolic, proteomic, and transcriptomic pattern that provides insight into the long-term consequences of cancer-induced remodeling. Specifically, we found that proteins involved in autophagy or proteasomal degradation machinery are increasingly expressed while structural proteins were decreased. Sirt1 has been found to drive autophagy via deacetylation and activation of FoxO3, a transcription factor that regulates the GTP-binding protein Rab7 and mediates autophagosome-lysosome fusion (Hariharan et al., 2010). Our analysis showed increased expression of lysosomal marker Lamp1 and FoxO3 at the protein and transcript levels. These findings suggest that initial metabolic response mechanisms that lead to activation of Sirt1 persist over time and induce a chronic activation of autophagy with broad metabolic and proteomic consequences.

Our data indicate that D2-HG treatment increases in both sexes the expression of proteins regulating chromatin organization, cytoskeleton organization, and cell signaling. These findings demonstrate the link between an initial metabolic response followed by targeted genome and proteome remodeling resulting in a new metabolic profile during prolonged adaptation. Further, our data show that the metabolic alterations induced by D2-HG affect the expression of proteins in a sex-dependent manner. Sex differences in muscle wasting and autophagy are increasingly recognized (Anderson et al., 2017; Miller et al., 2017; Montalvo et al., 2018; Yoon et al., 2018). Estrogens and androgens are important regulators of muscle mass and function (Spangenburg et al., 2012). Recent studies demonstrated that when autophagy is activated, acetylation of p300 is attenuated by Sirt1 or Sirt2 to modulate the degree of autophagic flux (Black et al., 2008; Han et al., 2008). Female mice are reported to have less basal ubiquitin-proteasome activity and greater autophagy activity compared to male mice (Cosper and Leinwand, 2011; Ogawa et al.,

2015), while male mice appear to differentially regulate Sirt2 activity in response to ischemia (Shimizu et al., 2016). Together our data provide evidence for sex-dependent etiologies for cancer cachexia development and the need to optimize therapies for skeletal muscle pathologies based on biological sex. The role of sex in regulating autophagy and muscle wasting requires further studies.

In conclusion, our findings shed new light on the mechanisms underlying the strong relationship between cancer and skeletal muscle loss by showing how oncometabolic stress activates autophagy. Our study points to a critical interplay between acetylation and deacetylation of proteins to regulate metabolic adaptation and proteome remodeling. It remains unclear how metabolic changes may impact epigenetic remodeling, and to what extent substrate replenishment can prevent the observed transcriptional and post-transcriptional changes. Our data clarify the importance of autophagy in cellular stress adaptation and provide insights into how metabolic changes drive autophagy activation. Understanding the molecular mechanisms that enable muscle cells to adapt and compensate for metabolic stress will be necessary for therapeutic strategies targeting metabolic pathways.

ACKNOWLEDGMENTS

We thank the Histopathology Laboratory, Department of Pathology and Laboratory Medicine, at McGovern Medical School at The University of Texas Health Science Center at Houston for generating histology samples. This work was supported by the American Heart Association (17POST33660221 to A.K.), the Burroughs Wellcome Fund (15RDM005 to A.K.) and National Institutes of Health (NIH) (R01-HL-061483 to H.T., K99-HL-141702 to A.K., R01-HL132075 and R01-HL144509 to R.A.G. and J.V.E. as co-PIs, K01-AI148593 to B.M.H.). The Metabolomics Core Facility at The University of Texas MD Anderson Cancer Center was supported by Cancer Prevention and Research Institute of Texas grant RP130397 and NIH grants S10OD012304-01, U01CA235510, and P30CA016672.

AUTHOR CONTRIBUTIONS

A.K. contributed to the conceptualization and project administration. A.K., J.V.E., B.M.H., P.L.L., R.G., H.T. contributed to the methodology. D.S., W.S, K.R. and J.V.E. (proteomics), A.K., L.T., and P.L.L. (metabolomics), A.K., A.Q.D., A.G., B.M.H. (transcriptomics) contributed to omic data generation and/or processing. H.V., W.S., D.M., H.B.B. and S.A. contributed to the microscopy and histology data collection. A.K., H.V., B.D.G. contributed to *in vitro* cell culture studies; A.K., R.S., B.D.G. contributed to *in vivo* mouse studies; A.K., D.T., R.G. contributed to seahorse analysis. A.K. contributed to data curation. A.K. and H.V. contributed to data visualization. A.K., B.M.H., D.S., K.R., D.T., P.L.L. contributed to omic data analysis. A.K. wrote and prepared the original draft.

DECLARATION OF INTERESTS

The authors declare no competing interests.

MAIN FIGURE TITLES AND LEGENDS

Figure 1. D2-HG causes metabolic remodeling in differentiated L6Ms.

(**A**) Schematic of *in vitro* experimental workflow and protocol.

(**B**) Oxygen consumption rate (OCR) of L6Ms in response to different D2-HG concentrations (0 to 1 mmol/L) was determined following sequential addition of oligomycin (OM, 1 µmol/L) to measure ATP-linked OCR, Carbonyl cyanide 4-(trifluoromethoxy)phenylhydrazone (FCCP, 0.2 µmol/L) to determine maximal respiration, and rotenone and antimycin (R/A, 1 µmol/L each) to determine the non-mitochondrial respiration as indicated. ATP-linked OCR and spare capacity were determined in L6Ms treated with the indicated dose of D2-HG (0 to 1 mmol/L) (*n* = 7 technical and biological replicates per group). Data are mean ± s.d. **P*-value<0.05, *****P*-value<0.0001. Statistical analysis using two-way ANOVA with post-hoc Tukey's multiple comparisons test.

(**C**) PCA of targeted metabolomics using LC-MS/MS in differentiated L6Ms treated with or without D2-HG (1 mmol/L) for 24 h. Each data point represents a biological replicate. Data is log2 normalized.

(**D**) Heatmap showing unsupervised hierarchical clustering of metabolites that are altered (*P*-value<0.05, FDR=10%) in the metabolomics dataset used in (B). The color-coded z-score illustrates the increase or decrease in metabolite concentrations upon D2-HG treatment.

(**E**) Network visualization of targeted MS-based metabolomics data. Nodes represent metabolites and edges represent metabolite-metabolite interactions. Nodes are color-coded by *P*-value and their size represent the median fold change relative to untreated sample.

Figure 2. Metabolic remodeling promotes activation of autophagy.

(**A** and **B**) Representative western blots of LC3-I, LC3-II, and the cytosolic marker GAPDH in total cell extracts from differentiated L6 myocytes (L6Ms) treated for 24 h with phosphate-buffered saline (PBS, control) or D2-HG (1 mmol/L). Cells were treated with or without bafilomycin A (BafA1, 200 nmol/L) for 2 h at the end of the 24 h culture. Densitometry analysis is shown below the representative blot (*n* = 3 independent experiments). Data are mean ± s.d. **P*-value<0.05, ***P*-value<0.01, ****P*-value<0.001. Statistical analysis using two-way ANOVA with post-hoc Tukey's multiple comparisons test.

(**C**-**D**) Gene expression of Map1-LC3B (**C**) and Murf1 (**D**) from differentiated L6 myocytes (L6Ms) treated for 24 h with phosphate-buffered saline (PBS, control) or D2-HG (1 mmol/L) (*n* = 8-10 independent experiments per group). Data are mean ± s.d. ***P*-value<0.01, ****P*-value<0.001, *****P*-value<0.0001. Statistical analysis using two-way ANOVA with post-hoc Tukey's multiple comparisons test.

(**E**-**F**) Representative live-cell images of L6Ms transfected with plasmid encoding a GFP-tagged LC3 (green) cultured with PBS, D2-HG (1 mmol/L) or BafA1 (200 nmol/L), and co-stained with LysoTracker (red). Puncta were counted for at least 100 cells per condition. Scale bars represent 10 µm. Data are mean ± s.d. ***P*-value<0.01, ****P*-value<0.001. Statistical analysis using two-way ANOVA with post-hoc Tukey's multiple comparisons test.

Figure 3. Deacetylation of LC3 is driven by Sirt1 in L6Ms.

(**A**) Schematic of Sirt1-mediated deacetylation of LC3.

(**B**) Representative western blotting depicting co-immunoprecipitation of LC3 and Sirt1 in differentiated L6Ms treated with or without D2-HG (1 mmol/L) for 24 h. Total expression of LC3-I, LC3-II, and GAPDH are depicted from 5% input of co-immunoprecipitation sample. Images are representative of n = 3 experiments.

(**C**) LC3 was immunoprecipitated from differentiated L6Ms expressing wild type LC3 and mutant LC3 with a lysine to arginine replacement at position 49 and 51, respectively. The degree of acetylation was assessed using pan-acetyl-lysine antibody. Both wild type and mutant LC3 expressing cells were treated with or without D2-HG (1 mmol/L) for 24 h.

(**D**) Representative live-cell images of L6Ms transfected with plasmid encoding a GFP-tagged LC3 (green) in wild type LC3 and mutant LC3 with a lysine to arginine replacement at position 49 and 51. Cells were treated with or without D2-HG (1 mmol/L) for 24 h, and puncta were counted for at least 100 cells per condition. Scale bars represent 10 µm. Data are mean ± s.d. ****P*-value<0.001, *****P*-value<0.0001.

(E) Representative western blotting of Sirt1, p300, and LC3-I and LC3-II expression in L6Ms.

(F and **G)** Silencing of Sirt1 expression (**F**) using siRNA and overexpression of p300 (**G**) reduces LC3-II level in differentiated L6Ms treated with D2-HG (*n* = 4 per group). Data are mean ± s.d. All *P*-values were determined by two-way analysis of variance (ANOVA).

Figure 4. *In vivo* changes in response to D2-HG.

(**A**) Experimental set-up to measure grip strength in mice. Mice are lifting weights ranging from 20 g to 90 g.

(**B**) Weight lifting scores in male and female mice treated with or without D2-HG (250 mg/kg body weight) over the course of the experiment (4 weeks). Scores are representative of the grip strength in mice and normalized by body weight (*n* = 4-5 mice per group and sex). Data are mean ± s.d. **P*-value<0.05. Statistical Analysis using a one unpaired t-test (two-step method by Benjamini, Krieger and Yekutieli) with a false discovery rate (FDR) of 5%.

(**C**) PCA of targeted metabolomics using LC-MS/MS in skeletal muscle from male (m) and female (f) mice treated with or without D2-HG (250 mg/kg body weight). Each data point represents a biological replicate. *n* = 4-5 mice per group and sex. Data is log2 normalized.

(**D**) Relative abundance of log2-normalized metabolites in male and female mice treated with or without D2-HG (250 mg/kg body weight). *n* = 4-5 mice per group and sex. Data are mean ± s.d. **P*-value<0.05. Statistical Analysis using a one unpaired t-test (two-step method by Benjamini, Krieger and Yekutieli) with a false discovery rate (FDR) of 5%.

Abbreviations: i.p., intra-peritoneal; MS, mass spectrometry; RNA-seq, RNA-sequencing; PCA, principal component analysis.

Figure 5. Multi-omics changes in response to D2-HG.

(**A**) Principal component analysis (PCA) of MS-based proteomics and RNA-sequencing (RNA-seq) of skeletal muscle tissue from male (m) and female (f) mice treated with or without D2-HG (250 mg/kg body weight). Each data point represents a biological replicate. *n* = 4-5 mice per group and sex. Data is log2 normalized.

(**B**) Enrichment analysis of significantly expressed proteins from MS-based proteomics using Gene Ontology (GO) annotations. The top-13 enriched terms after redundancy filtering were visualized according to negative log10 transformed FDR-values. The number of enriched genes is depicted by the size of each filled circle.

(**C**) STRING protein-protein analysis of significantly expressed proteins from MS-based proteomics. Nodes represent proteins and edges represent protein-protein interactions. Functional analysis of clusters obtained by Markov clustering. GO annotation from (**B**) were

visualized as split donut charts around the nodes. Proteins without any interaction partners within the network (singletons) are omitted from the visualization.

(**D**-**F**) Comparison of gene and protein expression in skeletal muscle tissue for Chromodomain-helicase-DNA-binding-protein 1 (Chd1) and histone 1.2 (H1.2) (**D**), lysosome-associated membrane glycoprotein 1 (Lamp1) and Bcl-2-associated athano gene 3 (Bag3) (**E**), and Sirtuin 2 (Sirt 2) and Dynein (**F**). *n* = 4-5 mice per group and sex. Data are mean ± s.d. **P*-value<0.05, ***P*-value<0.01, ****P*-value<0.001 and *****P*-value<0.0001. Statistical Analysis using a two-way ANOVA with a false discovery rate (FDR) of 5% for MS-proteomics and FDR of 1% for RNA-seq.

Figure 6. Integration of Multi-omics Analysis of Metabolite and Proteins.

(**A**) Principal component analysis (PCA) of MS-based targeted metabolomics skeletal muscle tissue from male (m) and female (f) mice treated with or without D2-HG (250 mg/kg body weight). Each data point represents a biological replicate (*n* = 4-5 mice per group and sex). Data is log2 normalized.

(**B**) Relative abundance of significantly up- or down-regulated metabolites in male and female mice treated with or without D2-HG. *n* = 4-5 mice per group and sex. Data are mean ± s.d. **P*-value<0.05, ***P*-value<0.01, ****P*-value<0.001. Statistical Analysis using a two-way ANOVA with a false discovery rate (FDR) of 5% for MS-metabolomics.

(**C**) Network analysis of targeted MS-based metabolomics data from skeletal muscle tissue. Nodes represent metabolites and edges represent metabolite-metabolite interactions. Nodes are color-coded by *P*-value and their size represent the median fold change relative to untreated control animals. Statistical Analysis using a two-way ANOVA with a false discovery rate (FDR) of 5% for MS-metabolomics.

(**D**) Pairwise Spearman correlation networks of multi-omics data based on MS-based proteomics and targeted MS-based metabolomics. Nodes represent metabolites and proteins, while edges represent metabolite-metabolite, protein-protein, and metabolite-protein interactions. Metabolites and proteins are depicted as squares or circles, respectively. Nodes were color-coded by *P*-value and size represents the median fold change relative to untreated control animals. Statistical Analysis using a cut-off of 0.75 for Spearman's rank correlation coefficient.

(**E**) Summary of the main discoveries.

Figure 1.

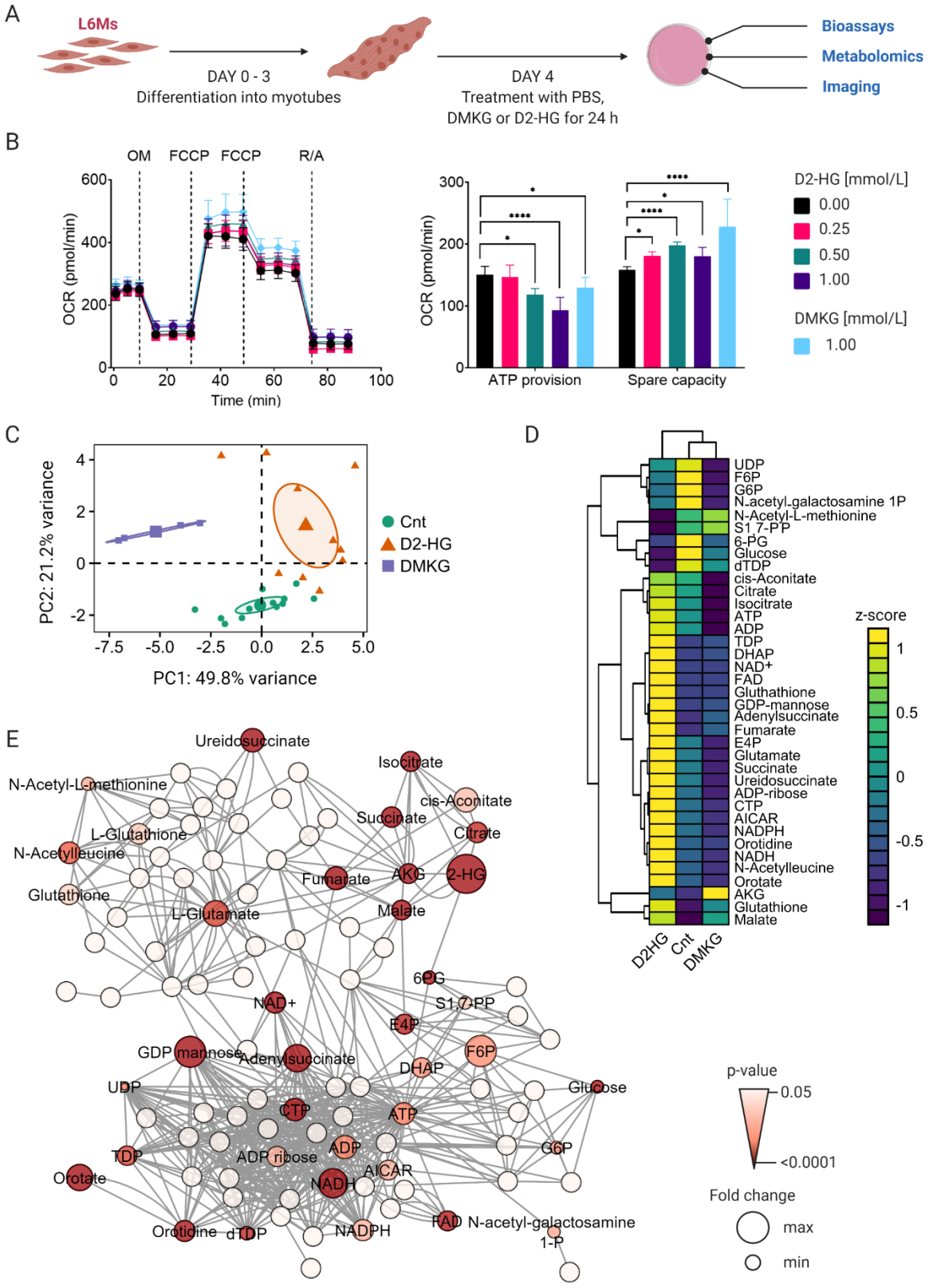
A
L6Ms
DAY 0 - 3
Differentiation into myotubes
DAY 4
Treatment with PBS,
DMKG or D2-HG for 24 h
Bioassays
Metabolomics
Imaging
B
OM
FCCP
FCCP
R/A
OCR (pmol/min)
Time (min)
ATP provision
Spare capacity
D2-HG [mmol/L]
0.00
0.25
0.50
1.00
DMKG [mmol/L]
1.00
C
PC2: 21.2% variance
PC1: 49.8% variance
Cnt
D2-HG
DMKG
D
z-score
D2HG
Cnt
DMKG
E
Ureidosuccinate
N-Acetyl-L-methionine
Isocitrate
cis-Aconitate
Succinate
Citrate
L-Glutathione
N-Acetylleucine
Fumarate
AKG
2-HG
Glutathione
L-Glutamate
Malate
6-PG
NAD+
S1,7-PP
E4P
GDP mannose
Adenylsuccinate
F6P
DHAP
UDP
Glucose
CTP
ATP
TDP
ADP ribose
ADP
G6P
Orotate
NADH
AICAR
Orotidine
dTDP
NADPH
FAD
N-acetyl-galactosamine 1-P
p-value
0.05
<0.0001
Fold change
max
min

Figure 2.

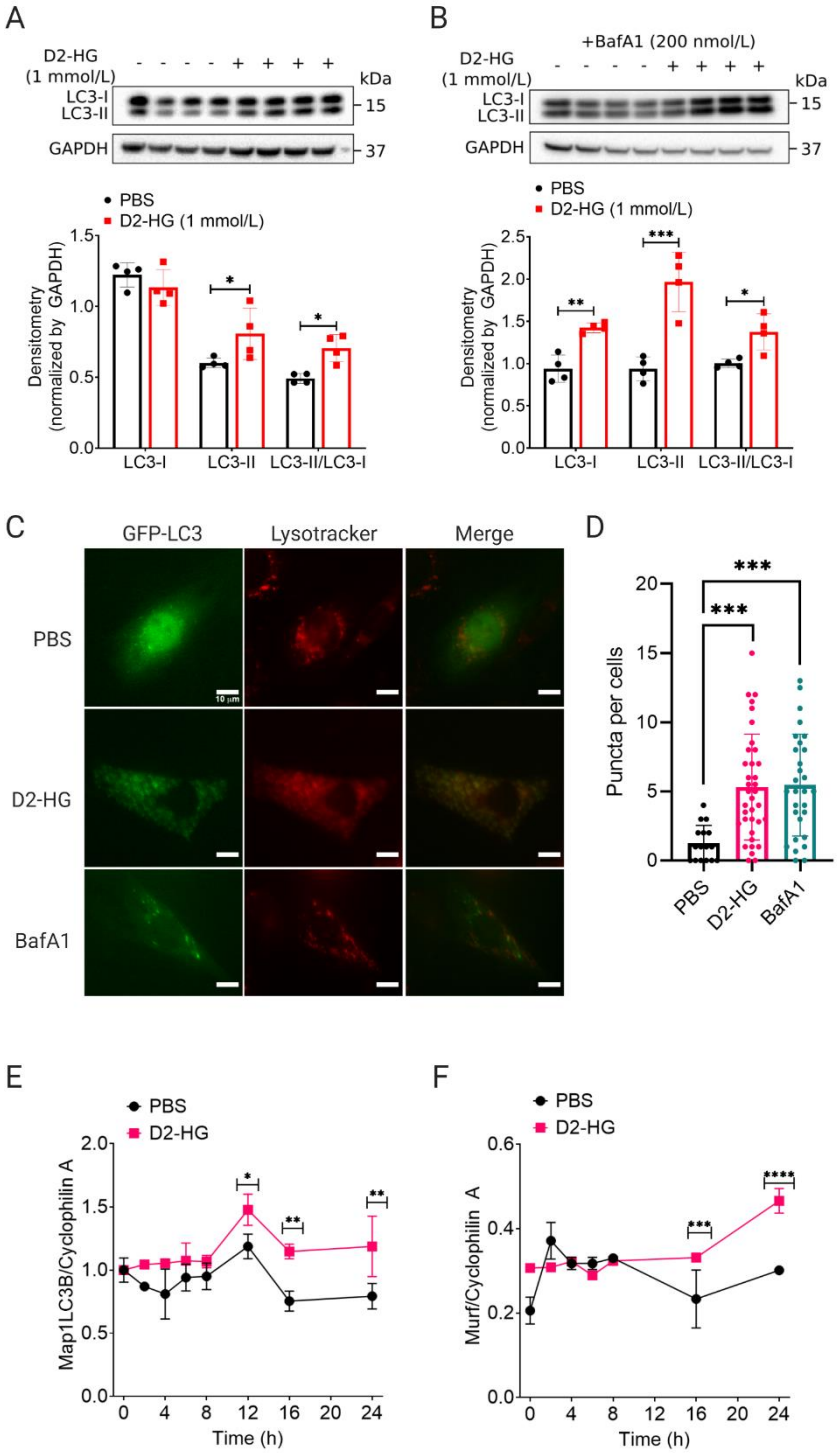
A
D2-HG (1 mmol/L)
- - - - + + + +
kDa
LC3-I
LC3-II
15
GAPDH
37
PBS
D2-HG (1 mmol/L)
Densitometry (normalized by GAPDH)
LC3-I
LC3-II
LC3-II/LC3-I
B
+BafA1 (200 nmol/L)
D2-HG (1 mmol/L)
- - - - + + + +
kDa
LC3-I
LC3-II
15
GAPDH
37
PBS
D2-HG (1 mmol/L)
Densitometry (normalized by GAPDH)
LC3-I
LC3-II
LC3-II/LC3-I
C
GFP-LC3
Lysotracker
Merge
PBS
D2-HG
BafA1
D
Puncta per cells
PBS
D2-HG
BafA1
E
PBS
D2-HG
Map1LC3B/Cyclophilin A
Time (h)
F
PBS
D2-HG
Murf/Cyclophilin A
Time (h)

Figure 3.

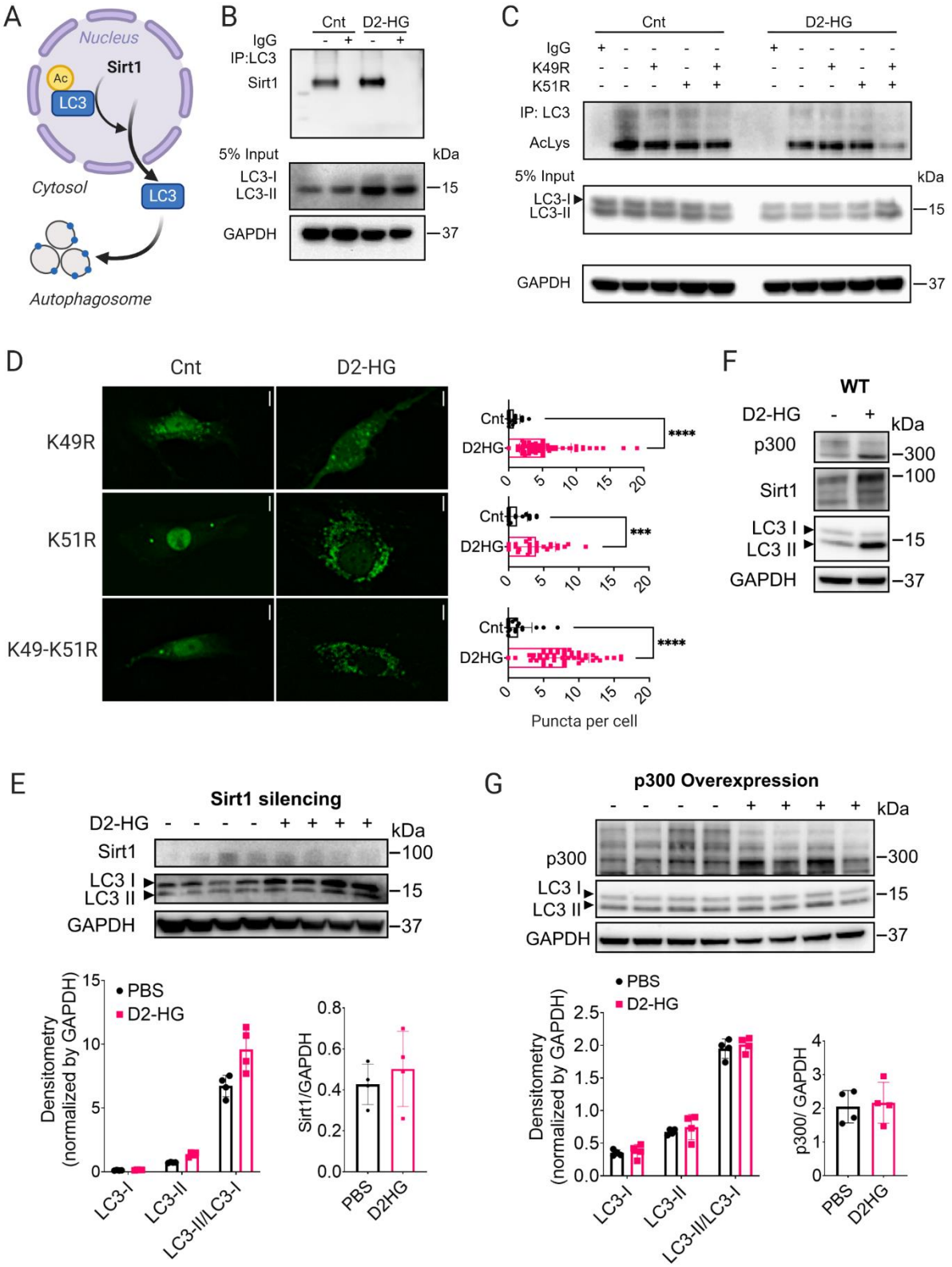
A
Nucleus
Sirt1
Ac
LC3
Cytosol
LC3
Autophagosome
B
Cnt
D2-HG
IgG
IP:LC3
Sirt1
5% Input
kDa
LC3-I
LC3-II
15
GAPDH
37
C
Cnt
D2-HG
IgG
K49R
K51R
IP: LC3
AcLys
5% Input
kDa
LC3-I
LC3-II
15
GAPDH
37
D
Cnt
D2-HG
K49R
K51R
K49-K51R
Cnt
D2HG
****
***
****
0
5
10
15
20
Puncta per cell
F
WT
D2-HG
kDa
p300
300
Sirt1
100
LC3 I
LC3 II
15
GAPDH
37
E
Sirt1 silencing
D2-HG
kDa
Sirt1
100
LC3 I
LC3 II
15
GAPDH
37
PBS
D2-HG
Densitometry (normalized by GAPDH)
LC3-I
LC3-II
LC3-II/LC3-I
Sirt1/GAPDH
PBS
D2HG
G
p300 Overexpression
kDa
p300
300
LC3 I
LC3 II
15
GAPDH
37
PBS
D2-HG
Densitometry (normalized by GAPDH)
LC3-I
LC3-II
LC3-II/LC3-I
p300/ GAPDH
PBS
D2HG

Figure 4.

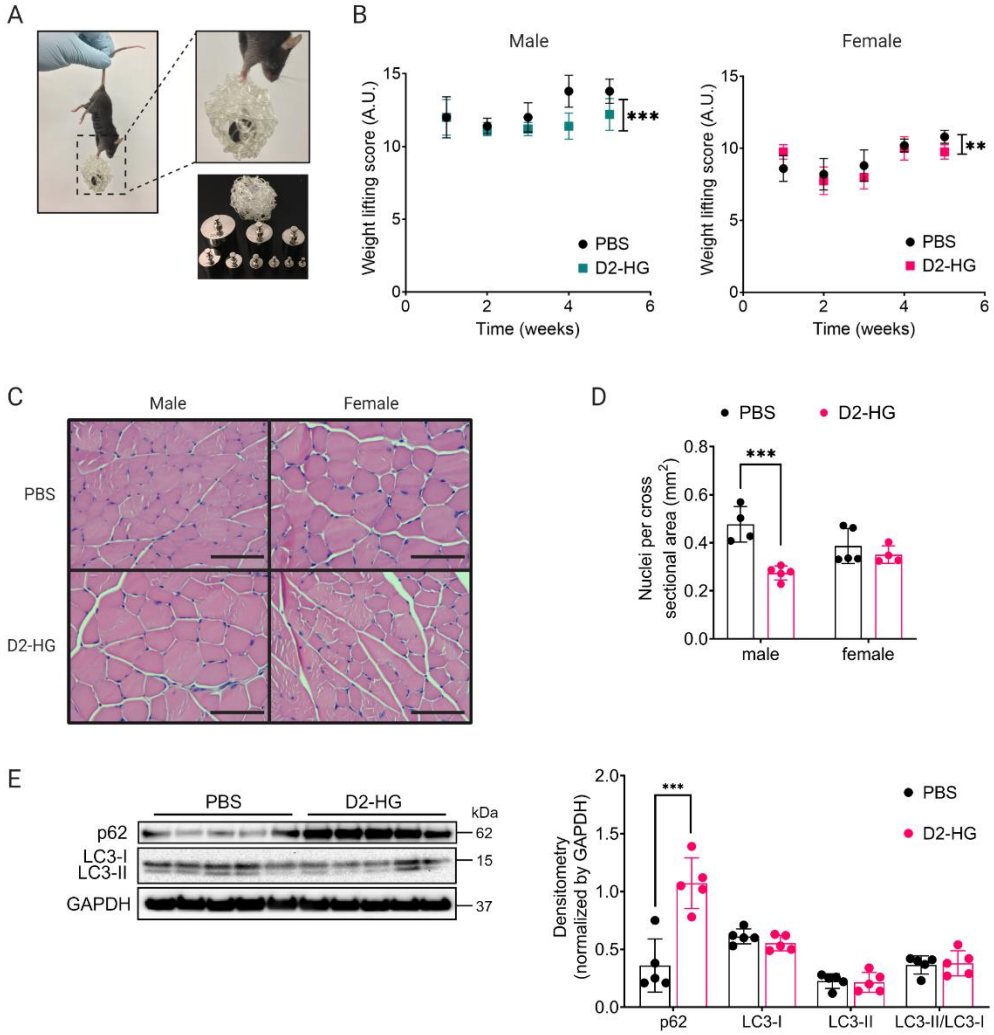
A
B
Male
Female
Weight lifting score (A.U.)
Time (weeks)
PBS
D2-HG
***
**
C
Male
Female
PBS
D2-HG
D
PBS
D2-HG
Nuclei per cross sectional area (mm^2)
male
female
E
PBS
D2-HG
kDa
p62
LC3-I
LC3-II
GAPDH
62
15
37
Densitometry (normalized by GAPDH)
p62
LC3-I
LC3-II
LC3-II/LC3-I

Figure 5.

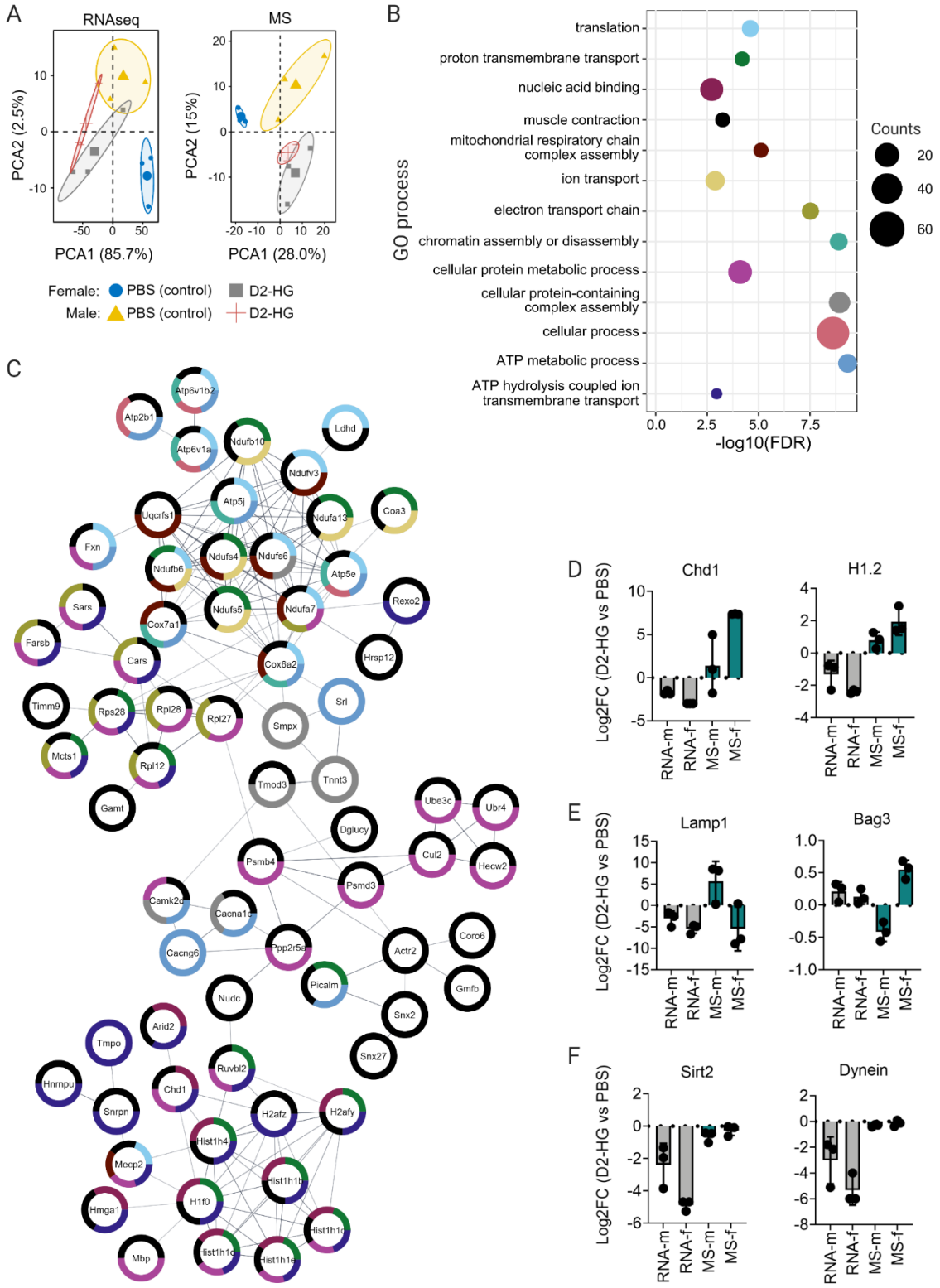
A
RNAseq
MS
PCA2 (2.5%)
PCA1 (85.7%)
PCA2 (15%)
PCA1 (28.0%)
Female: PBS (control) D2-HG
Male: PBS (control) D2-HG
B
translation
proton transmembrane transport
nucleic acid binding
muscle contraction
mitochondrial respiratory chain complex assembly
ion transport
electron transport chain
chromatin assembly or disassembly
cellular protein metabolic process
cellular protein-containing complex assembly
cellular process
ATP metabolic process
ATP hydrolysis coupled ion transmembrane transport
GO process
-log10(FDR)
Counts
20
40
60
C
D
Chd1
H1.2
E
Lamp1
Bag3
F
Sirt2
Dynein
Log2FC (D2-HG vs PBS)
RNA-m
RNA-f
MS-m
MS-f

Figure 6.

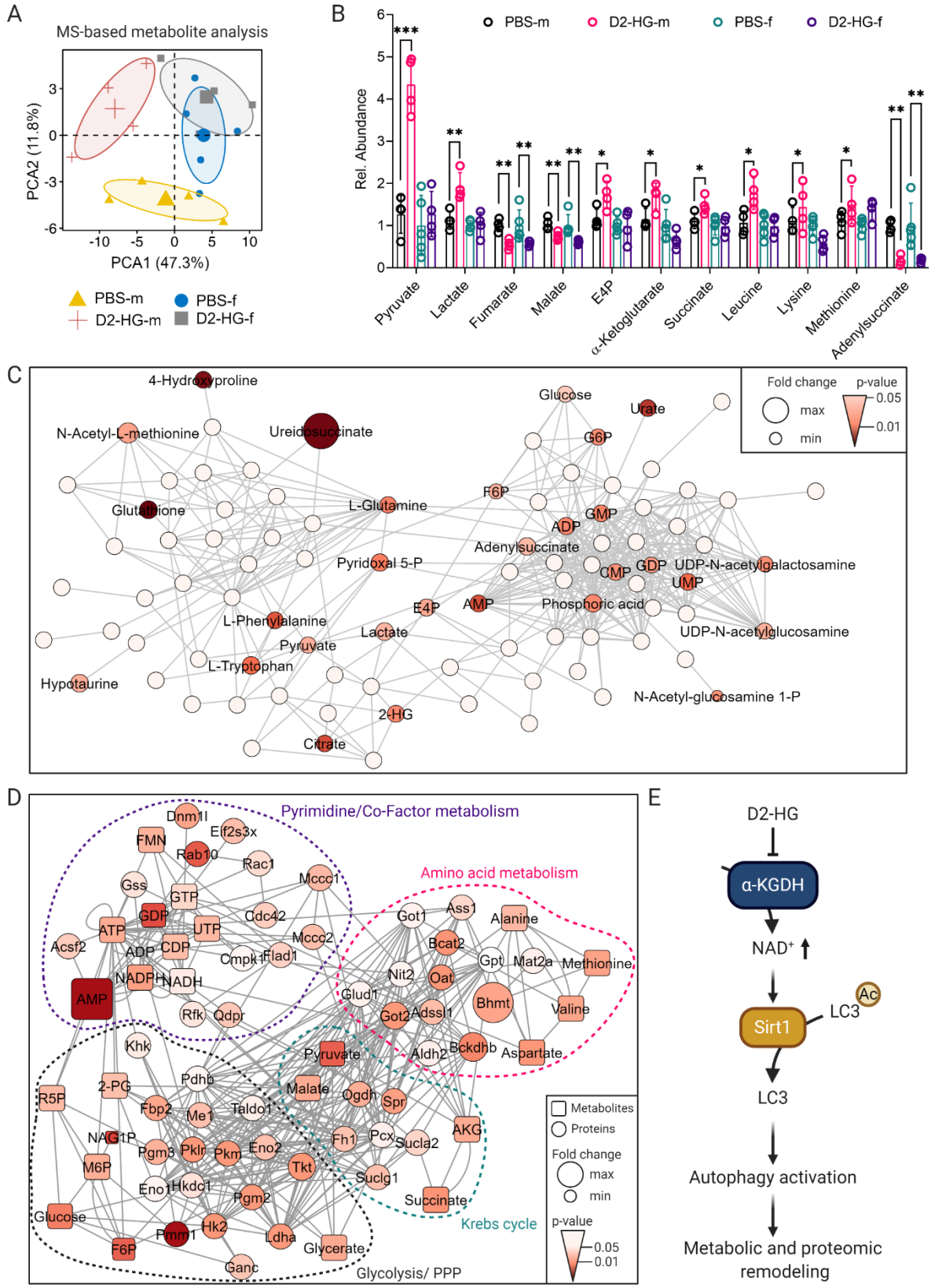
A
MS-based metabolite analysis
PCA2 (11.8%)
PCA1 (47.3%)
PBS-m
D2-HG-m
PBS-f
D2-HG-f
B
PBS-m
D2-HG-m
PBS-f
D2-HG-f
Rel. Abundance
Pyruvate
Lactate
Fumarate
Malate
E4P
α-Ketoglutarate
Succinate
Leucine
Lysine
Methionine
Adenylsuccinate
C
Fold change
p-value
max
min
0.05
0.01
4-Hydroxyproline
N-Acetyl-L-methionine
Ureidosuccinate
Glucose
Urate
G6P
F6P
Glutathione
L-Glutamine
GMP
ADP
Adenylsuccinate
Pyridoxal 5-P
CMP
GDP
UDP-N-acetylgalactosamine
UMP
E4P
AMP
Phosphoric acid
L-Phenylalanine
Lactate
UDP-N-acetylglucosamine
Pyruvate
L-Tryptophan
Hypotaurine
N-Acetyl-glucosamine 1-P
2-HG
Citrate
D
Pyrimidine/Co-Factor metabolism
Amino acid metabolism
Krebs cycle
Glycolysis/ PPP
Metabolites
Proteins
Fold change
max
min
p-value
0.05
0.01
E
D2-HG
α-KGDH
NAD+
Sirt1
Ac
LC3
LC3
Autophagy activation
Metabolic and proteomic remodeling

SUPPLEMENTAL FIGURE TITLES AND LEGENDS

Figure S1. Metabolic impact of D2-hydroxyglutarate (D2-HG) on mitochondrial function and α-Ketoglutarate concentration, Related to Figure 1.

(**A**) Oxygen consumption rate (OCR) of differentiated L6Ms treated with or without D2-HG was determined following sequential addition of oligomycin (OM, 1 μmol/L) to measure ATP-linked OCR (ATP-provision), Carbonyl cyanide 4-(trifluoromethoxy)phenylhydrazone (FCCP, 0.2 μmol/L) to determine maximal respiration, and rotenone and antimycin (R/A, 1 μmol/L each) to determine the non-mitochondrial respiration as indicated (*n* = 7 technical and biological replicates per group). Data are mean ± s.d. **P*-value<0.05, *****P*-value<0.0001. All *P*-values determined by two-way analysis of variance (ANOVA) with Sidak-Holms test to correct for multiple comparisons.

(**B**) Measurement of α-Ketoglutarate level in differentiated L6Ms treated with or without D2-HG (1 mmol/L), dimethyl α-Ketoglutarate (DMKG, 1 mmol/L) and bis 2-(5phenylacetamido-1,3,4,-thiadiazol-2-yl)ethyl-sulfide),(2-bromoethyl) trimethylammonium bromide (BPTES, 20 μmol/L) for 24 h (*n* = 4-8 independent experiments per group).

Data are mean ± s.d. All *P*-values determined by one-way analysis of variance (ANOVA) with Dunnett's test to correct for multiple comparisons.

Figure S2. Activation of autophagy in response to D2-HG, Related to Figure 2.

(**A-B**) Western blots of LC3-I and LC3-II in differentiated L6 myocytes (L6Ms) treated with or without DMKG (DMKG, 1.0 mmol/L) and bafilomycin A1 (200 nmol/L). GAPDH was used as a loading control (*n* = 5 independent experiments per group).

(**C-E**) mRNA expression of Mafbx1 (**C**), Beclin1 (**D**), and p62 (**E**) in L6Ms treated with or without D2-HG.

Data are mean ± s.d. All *P*-values determined by two-way analysis of variance (ANOVA) with Tukey's test for multiple comparisons.

Figure S3. D2-HG-induced autophagy is driven by the deacetylation of LC3, Related to Figure 3.

(**A**-**B**) Western blots of total AMPK and mTOR, and phosphorylated AMPK and mTOR in differentiated L6 myocytes (L6Ms) treated with or without D2-HG (1 mmol/L) for 24 h. The expression of LC3 was determined using western blotting after treatment with or without the lysosomal inhibitor bafilomycin (BafA1, 20 nmol/L; for 2 h). GAPDH was used as a loading control (*n* = 5 independent experiments per group).

(**C**-**D**) LC3 was immunoprecipitated from differentiated L6Ms expressing wild type LC3 and mutant LC3 with lysine to glutamine replacement at position 49 and 51, respectively. The degree of acetylation was assessed using a pan-acetyl-lysine antibody. Both wild type and mutant LC3 expressing cells were treated with or without D2-HG (1 mmol/L) for 24 h.

All data are mean ± s.d. Statistical analysis was conducted by two-way analysis of variance (ANOVA) with Tukey's test for multiple comparisons.

Figure S4. D2-HG promotes skeletal muscle atrophy *in vivo,* Related to Figure 4.

(**A**) Schematic for the experimental protocol (Abbreviation: bwt, bodyweight).

(**B**-**C**) Bodyweight (**B**) and *M. gastrocnemius* weight (**C**) normalized by tibia length of mice treated with PBS (control) and D2-HG (*n* = 4-5 mice per group and sex). Data are mean ± s.d. Statistical analysis by two-way analysis of variance (ANOVA). ***P*-value<0.01.

(**D**) The relative abundance of 2-Hydroxyglutarate, normalized to the PBS-treated male and female group (*n* = 4-5 mice per group and sex).

Data are mean ± s.d. ***P*-value<0.01.

Figure S5. Multi-omics changes in response to D2-HG, Related to Figure 5.

(**A**) Experimental design – whole skeletal muscle tissue from male and female mice were analyzed using RNA-sequencing (RNA-seq), mass spectrometry (MS) based targeted metabolomics, and MS-based untargeted proteomics using the IN-sequence workflow (see Methods for details).

(**B**) The volcano plot shows negative log10 enrichment *P* values and log2 fold changes in the differential expression results of RNA-seq (left panel) and MS-proteomics.

(**C**-**D**) Unsupervised hierarchical clustering of significantly expressed (**C**) genes (FDR<1%; -1.5 ≦ fold-change ≧ 1.5) and (**D**) proteins (FDR<5%; -1.5 ≦ fold-change ≧ 1.5).
Expression values are log2-normalized and z-scored. Statistical analysis using two-way ANOVA (two-sided) with Tukey's posthoc test for multiple corrections.

Figure S6. Correlation and two-dimensional annotation enrichment analysis of transcriptomics and proteomics data, Related to Figure 5.

(**A**) Correlation between transcriptomics and proteomics data in skeletal muscle tissue from male and female mice treated for 30-days with D2-HG (250 mg/kg body weight). Data are log2-transformed and were corrected for sex, as well as batch effects. Proteins showing corresponding regulation at the genome and proteome level are depicted in red, while proteins with only significant regulation at the protein level are depicted in blue.

(**B**-**C**) Two-dimensional annotation enrichment analysis based on transcriptome (RNA-sequencing) and proteome expression in skeletal muscle tissue from (B) female and (C) male mice treated with D2-HG for 30-days. Significant metabolic pathways (KEGG and Reactome) and gene ontology terms are distributed along the proteome and transcriptome change direction. Female and male mice show differentially up- or down-regulated metabolic pathways in response to D2-HG treatment *in vivo*. Types of databases used for annotations are color-coded as depicted in the legend.

Figure S7. Mass spectrometry-based targeted metabolomic analysis of skeletal muscle tissue in response to D2-HG, Related to Figure 6.

(**A**) Hierarchical clustering of relative metabolite abundance in skeletal muscle tissue in female (f) or male (m) mice treated with phosphate-buffered saline (PBS) or D2-HG (250 mg/ kg body weight) for 30-days. Abundances were normalized using z-score. Clustering performed using 1-Pearson's correlation and average linkage.

(**B**) Composition of clusters in MS-based metabolomics using Reactome pathway knowledgebase. (**C**) Comparison of correlation analysis of MS-based proteomics and metabolomics data using Spearman's rank correlation and Pearson correlation coefficient.

Figure S1.

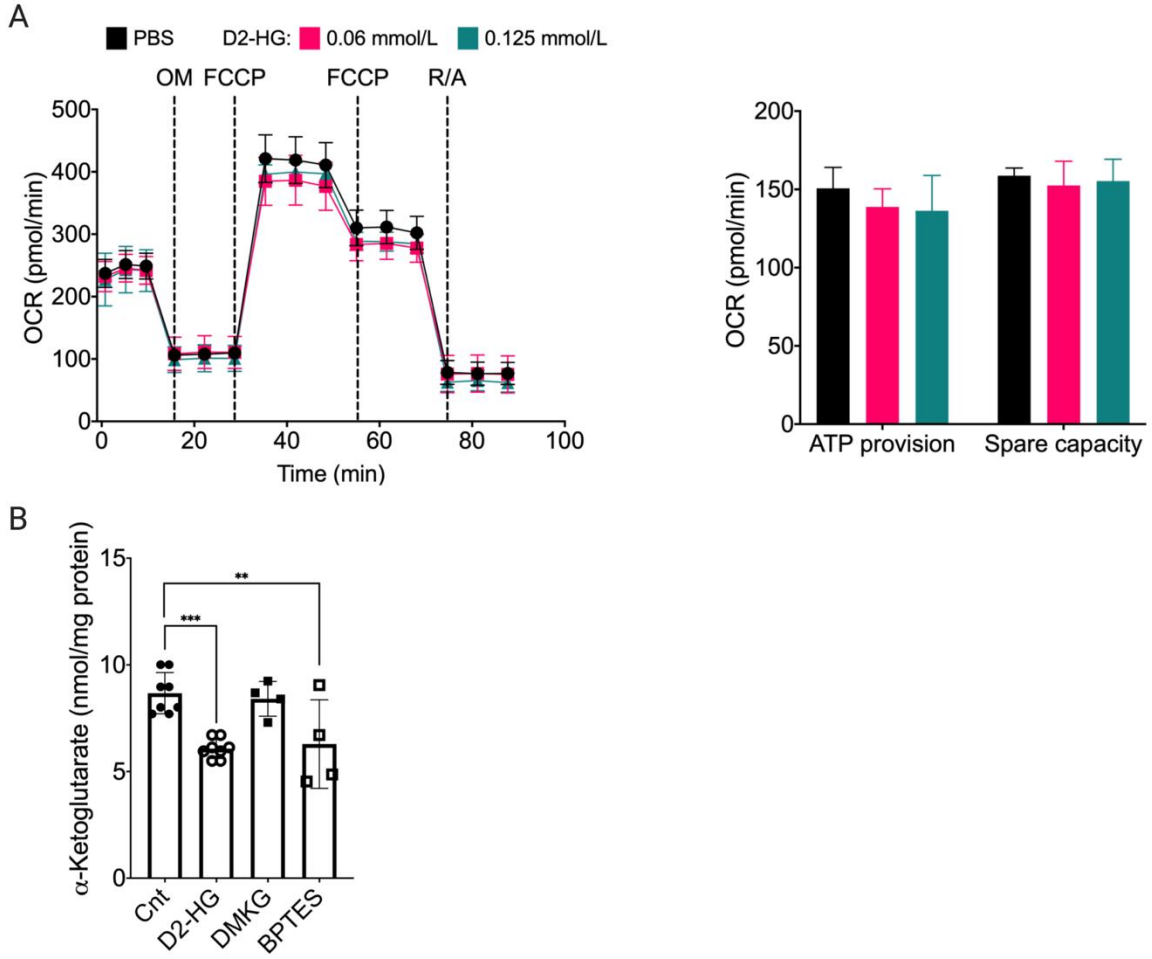
A
PBS
D2-HG: 0.06 mmol/L
0.125 mmol/L
OM
FCCP
FCCP
R/A
OCR (pmol/min)
Time (min)
ATP provision
Spare capacity
B
α-Ketoglutarate (nmol/mg protein)
Cnt
D2-HG
DMKG
BPTES

Figure S2.

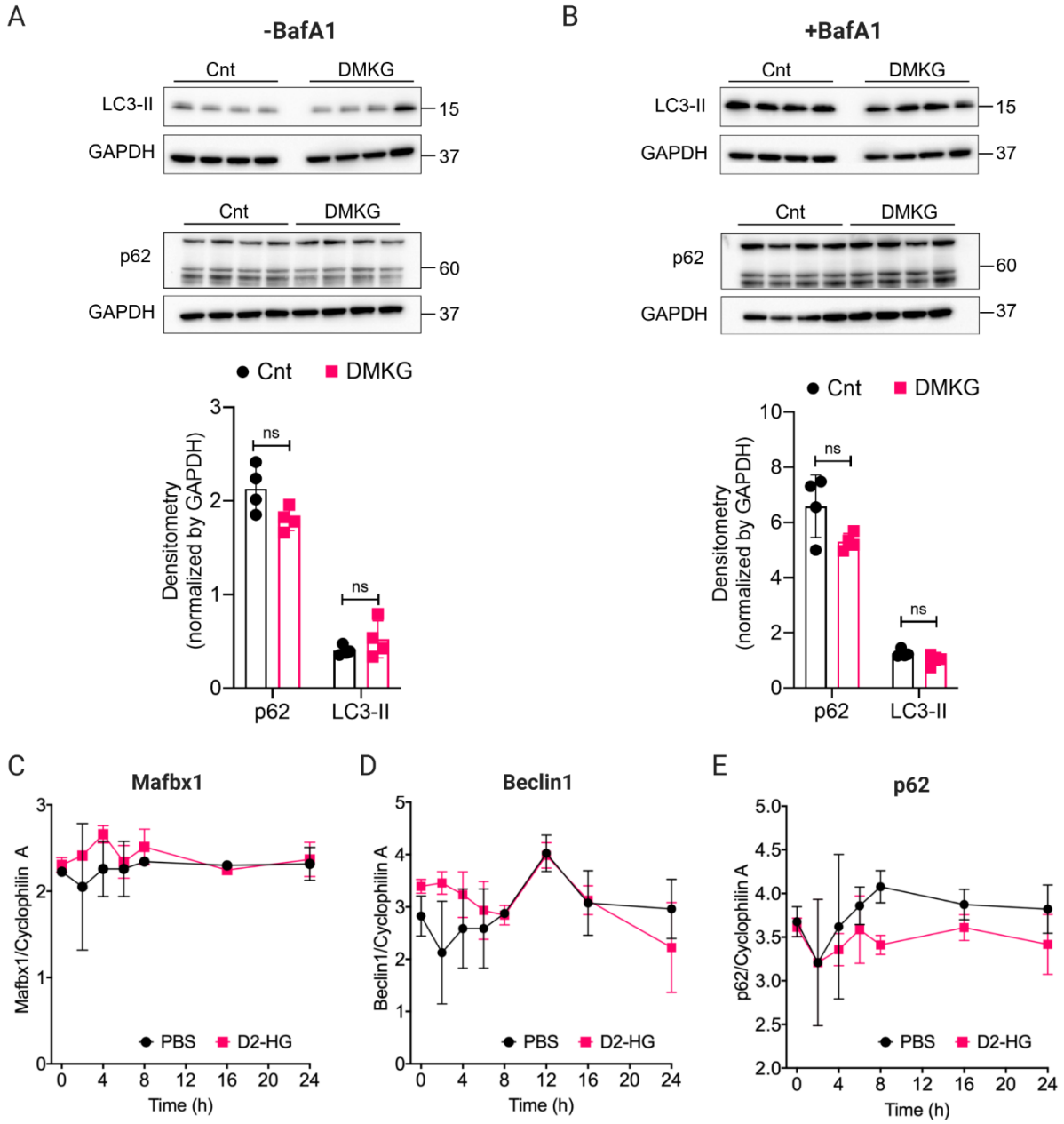
A
-BafA1
Cnt
DMKG
LC3-II
GAPDH
15
37
p62
60
Cnt
DMKG
Densitometry (normalized by GAPDH)
ns
p62
LC3-II
B
+BafA1
C
Mafbx1
Mafbx1/Cyclophilin A
PBS
D2-HG
Time (h)
D
Beclin1
Beclin1/Cyclophilin A
E
p62
p62/Cyclophilin A

Figure S3.

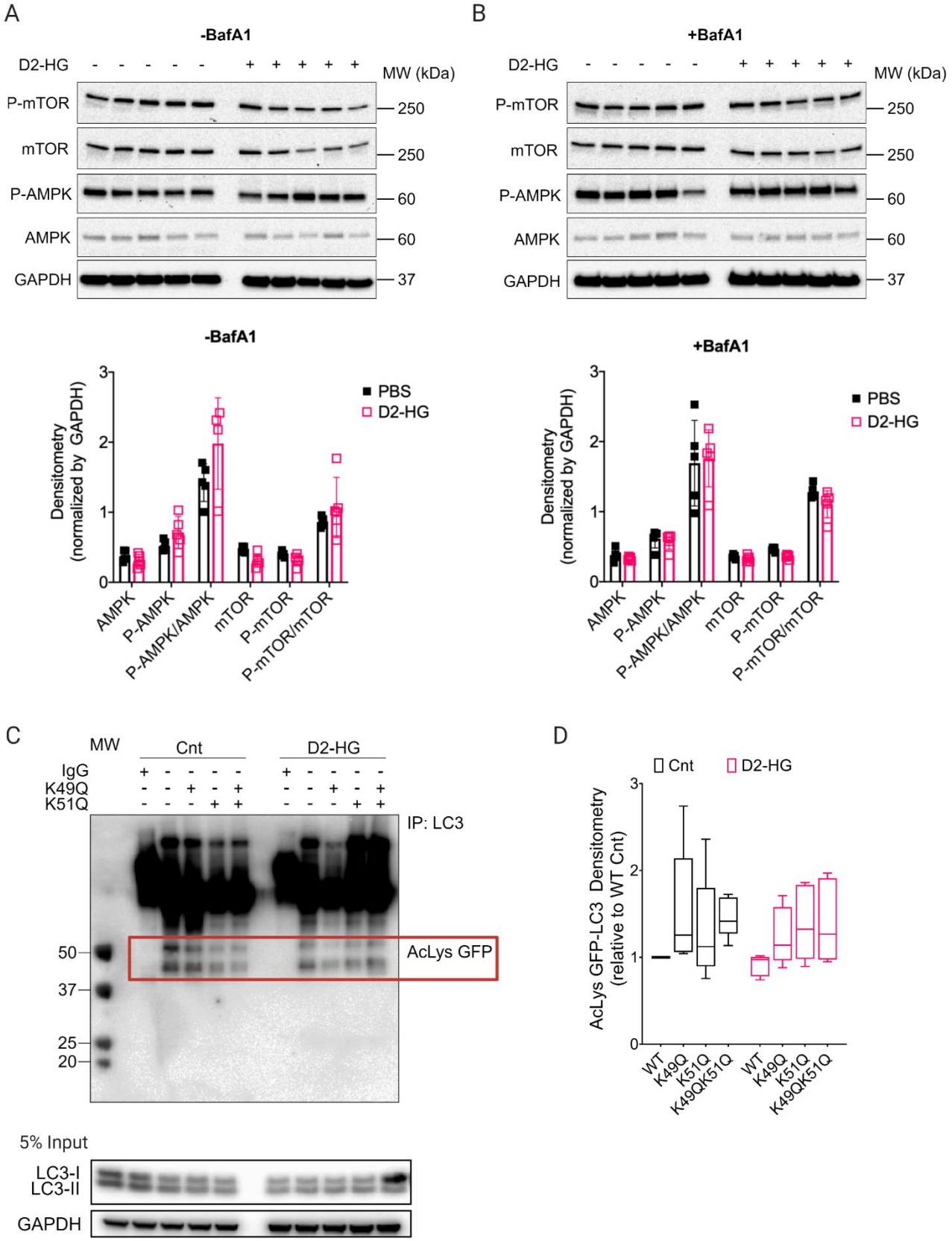
A
-BafA1
D2-HG
MW (kDa)
P-mTOR
mTOR
P-AMPK
AMPK
GAPDH
250
250
60
60
37
B
+BafA1
Densitometry (normalized by GAPDH)
PBS
D2-HG
AMPK
P-AMPK
P-AMPK/AMPK
mTOR
P-mTOR
P-mTOR/mTOR
C
MW
Cnt
D2-HG
IgG
K49Q
K51Q
IP: LC3
AcLys GFP
50
37
25
20
5% Input
LC3-I
LC3-II
GAPDH
D
Cnt
D2-HG
AcLys GFP-LC3 Densitometry (relative to WT Cnt)
WT
K49Q
K51Q
K49QK51Q

Figure S4.

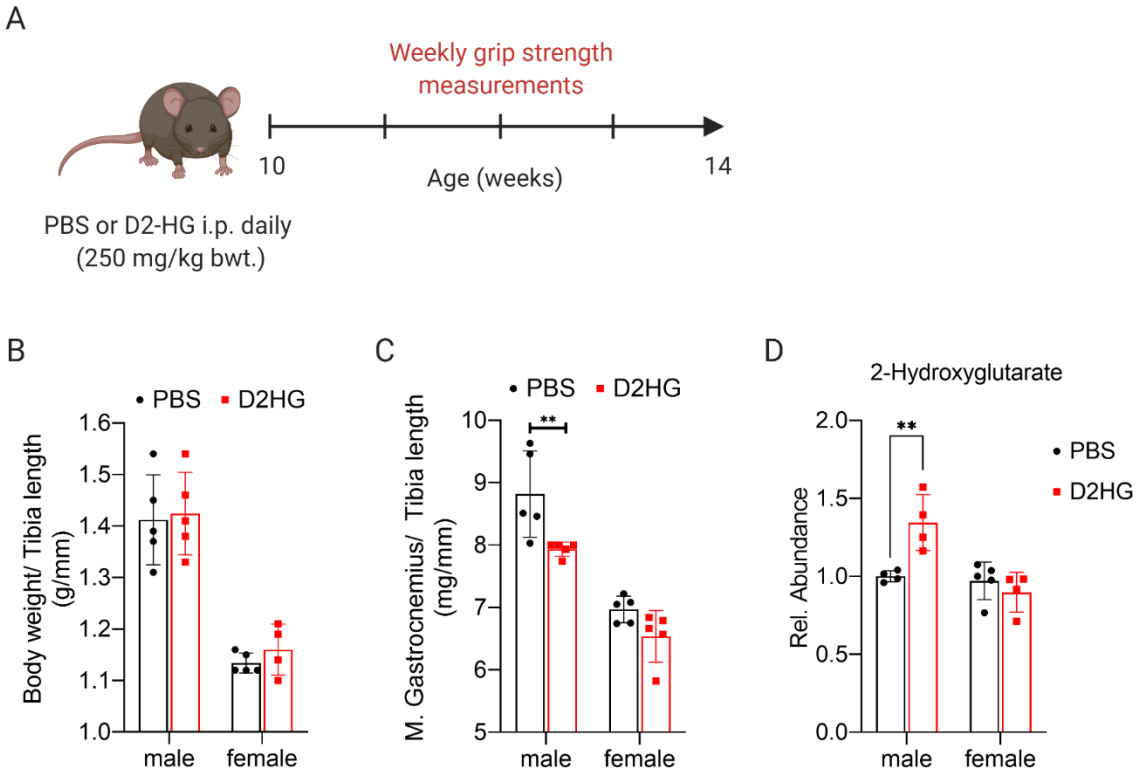
A
Weekly grip strength measurements
10
Age (weeks)
14
PBS or D2-HG i.p. daily (250 mg/kg bwt.)
B
PBS
D2HG
Body weight/ Tibia length (g/mm)
1.6
1.5
1.4
1.3
1.2
1.1
1.0
male
female
C
PBS
D2HG
M. Gastrocnemius/ Tibia length (mg/mm)
10
9
8
7
6
5
**
male
female
D
2-Hydroxyglutarate
Rel. Abundance
2.0
1.5
1.0
0.5
0.0
**
PBS
D2HG
male
female

Figure S5.

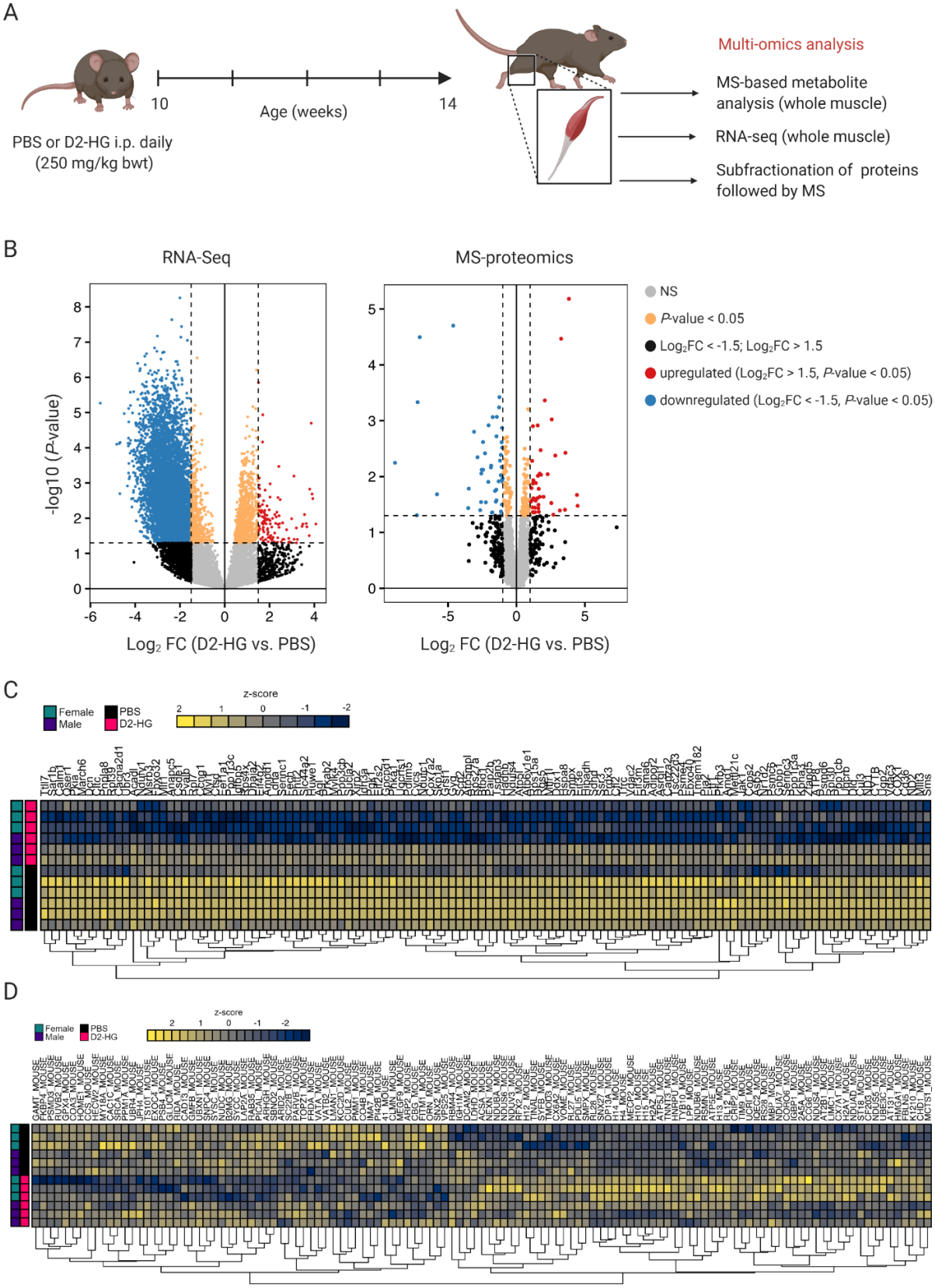
A
10
Age (weeks)
14
PBS or D2-HG i.p. daily
(250 mg/kg bwt)
Multi-omics analysis
MS-based metabolite analysis (whole muscle)
RNA-seq (whole muscle)
Subfractionation of proteins followed by MS
B
RNA-Seq
MS-proteomics
-log10 (P-value)
Log2 FC (D2-HG vs. PBS)
NS
P-value < 0.05
Log2FC < -1.5; Log2FC > 1.5
upregulated (Log2FC > 1.5, P-value < 0.05)
downregulated (Log2FC < -1.5, P-value < 0.05)
C
Female
Male
PBS
D2-HG
z-score
D

Figure S6.

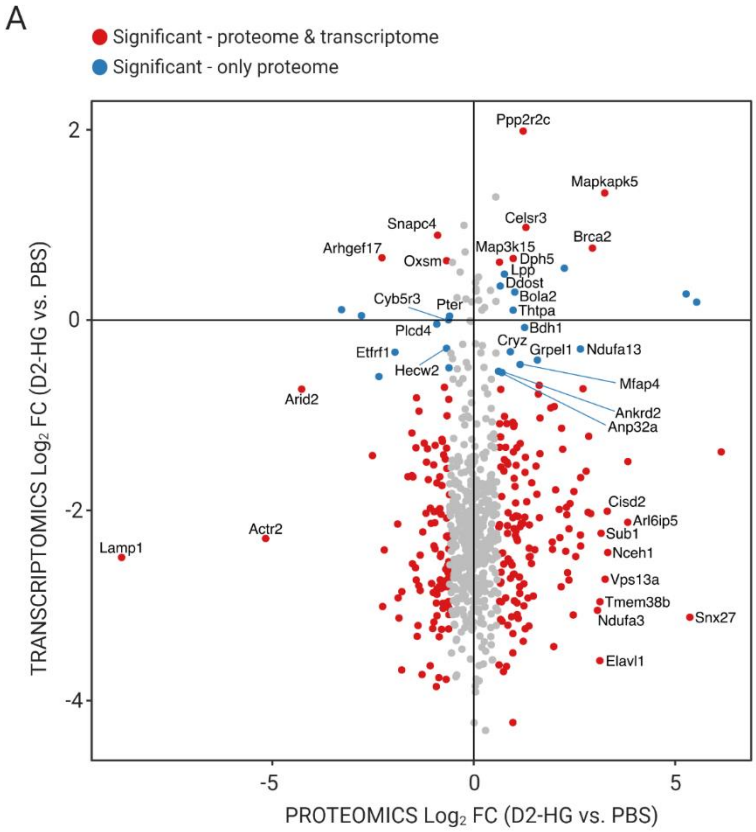

Actr2 Agpat3 AI837181 Akr1e1 Alyref Angptl7 Anp32b Aoc3 Arhgdib Arhgef17 Arid2 Arl6ip5 Arl8b Atad1 Atp2a2 Atp5l Atp6v1b2 Bcam Brca2 Cacybp Camk2d Cd36 Celsr3 Cilp2 Cisd2 Cnpy2 Col6a6 Cops8 Cox6a2 Crocc Csrp3 Cst3 Ddt Dnaja4 Dnajb5 Eif3l Eif3m Eif4g2 Elavl1 Ensa Epm2aip1 Etfdh Fam162a Fam213a Fundc2 Ggct Gnai2 Gstt1 Hddc2 Hnrnpu Hook3 Hprt Hspb8 Immt Lama4 Lamp1 Lamtor1 Lemd2 Letm1 Lman1 Lrpap1 Lzic Mapkapk5 Mb Mbp Mecp2 Mlip Mob1a Mpc2 Mydg Myl2 Myo1c Myoz2 Nceh1 Ndufa13 Ndufa13 Ndufa3 Ndufb3 Ndufb9 Ndufs5 Ndufv3 Nrap Nxn Pank4 Pcp4l1 Pex19 Pon3 Postn Ppp2r2c Pptc7 Prmt5 Prr12 Psap Psmb4 Psmc6 Psmd4 Pura Rab12 Rpl29 S100a1 Sacm1l Scrib Sec22b Sfpq Sfxn3 Smtnl1 Snx27 Stbd1 Sub1 Sun2 Svil Sypl Tcap Timm44 Timm50 Timm8a1 Tinagl1 Tmem38b Tmem43 Tmsb4x Tnni1 Tns3 Tomm40 Tpp1 Trappc3 Twf2 Ube2f Ubqln2 Uchl1 Vps13a Vps37c Wfs1 Xirp2 Ykt6

Aimp2 Ankrd2 Anp32a Appl1 Bdh1 Bola2 Cfap100 Cryz Cstf3 Cyb5r3 Ddost Eif5b Etfrf1 Fanci Grpel1 Hecw2 Lpp Mfap4 Ndufa13 Ndufa13 Pdcd11 Plcd4 Pter Thtpa

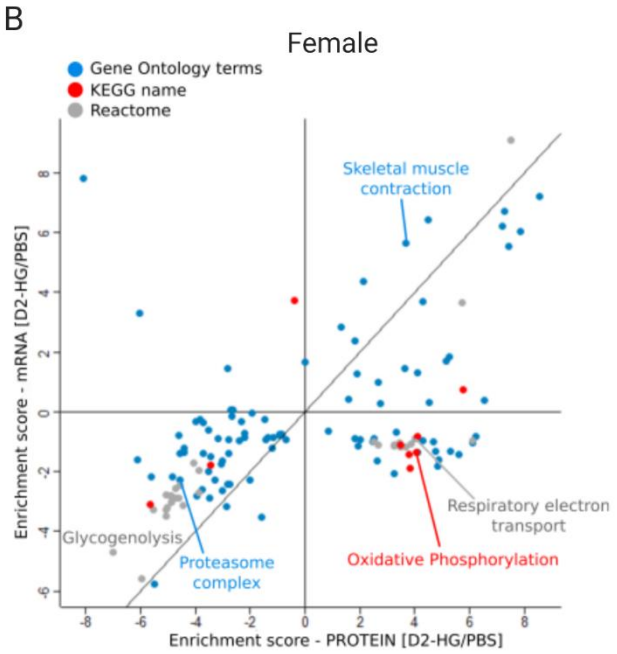

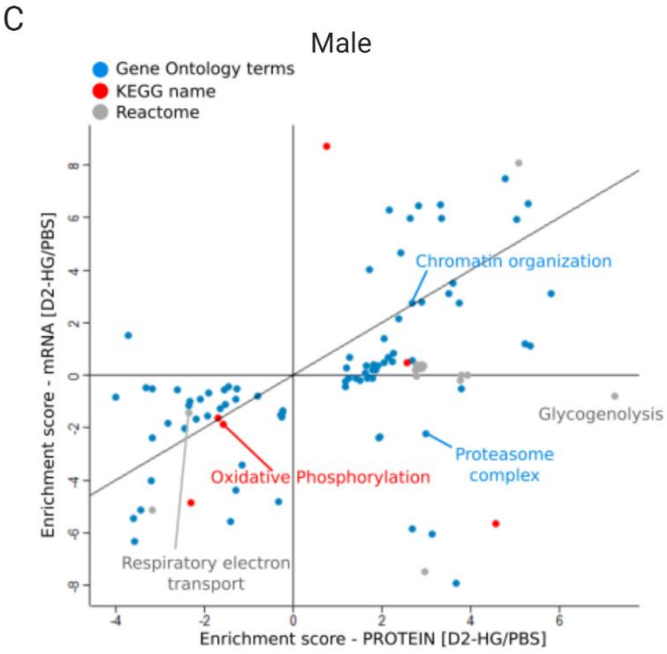

Figure S7.

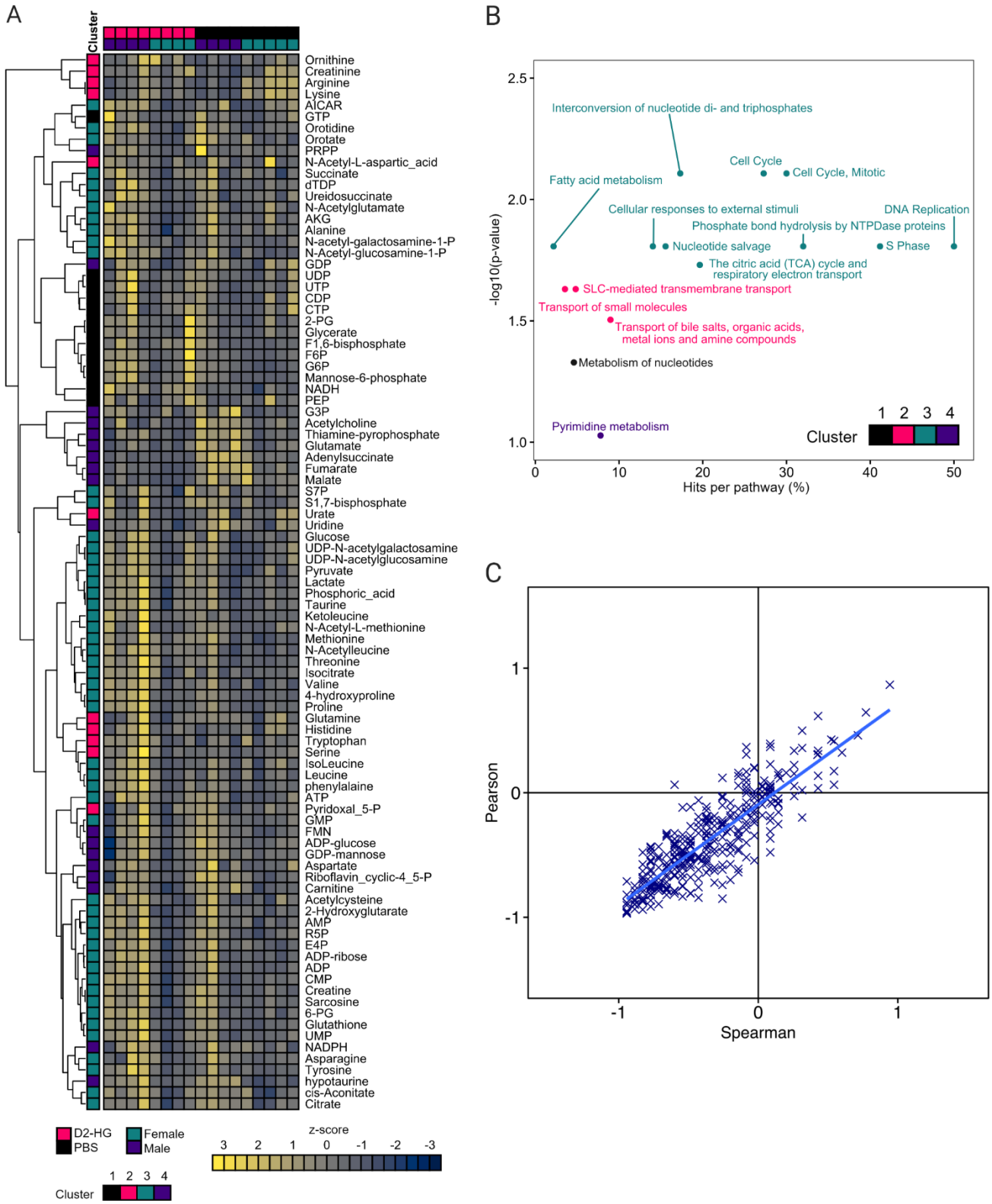
A
Cluster
Ornithine
Creatinine
Arginine
Lysine
AICAR
GTP
Orotidine
Orotate
PRPP
N-Acetyl-L-aspartic_acid
Succinate
dTDP
Ureidosuccinate
N-Acetylglutamate
AKG
Alanine
N-acetyl-galactosamine-1-P
N-Acetyl-glucosamine-1-P
GDP
UDP
UTP
CDP
CTP
2-PG
Glycerate
F1,6-bisphosphate
F6P
G6P
Mannose-6-phosphate
NADH
PEP
G3P
Acetylcholine
Thiamine-pyrophosphate
Glutamate
Adenylsuccinate
Fumarate
Malate
S7P
S1,7-bisphosphate
Urate
Uridine
Glucose
UDP-N-acetylgalactosamine
UDP-N-acetylglucosamine
Pyruvate
Lactate
Phosphoric_acid
Taurine
Ketoleucine
N-Acetyl-L-methionine
Methionine
N-Acetylleucine
Threonine
Isocitrate
Valine
4-hydroxyproline
Proline
Glutamine
Histidine
Tryptophan
Serine
IsoLeucine
Leucine
phenylalaine
ATP
Pyridoxal_5-P
GMP
FMN
ADP-glucose
GDP-mannose
Aspartate
Riboflavin_cyclic-4_5-P
Carnitine
Acetylcysteine
2-Hydroxyglutarate
AMP
R5P
E4P
ADP-ribose
ADP
CMP
Creatine
Sarcosine
6-PG
Glutathione
UMP
NADPH
Asparagine
Tyrosine
hypotaurine
cis-Aconitate
Citrate
D2-HG
PBS
Female
Male
z-score
3 2 1 0 -1 -2 -3
1 2 3 4
Cluster
B
Interconversion of nucleotide di- and triphosphates
Cell Cycle
Cell Cycle, Mitotic
Fatty acid metabolism
Cellular responses to external stimuli
DNA Replication
Phosphate bond hydrolysis by NTPDase proteins
Nucleotide salvage
S Phase
The citric acid (TCA) cycle and respiratory electron transport
SLC-mediated transmembrane transport
Transport of small molecules
Transport of bile salts, organic acids, metal ions and amine compounds
Metabolism of nucleotides
Pyrimidine metabolism
-log10(p-value)
Hits per pathway (%)
1 2 3 4
Cluster
C
Pearson
Spearman

METHODS

In vivo animal studies.

All animal experiments were conducted according to the Institutional Animal Care and Use Committee and conducted in accordance with the guidelines issued by The University of Texas Health Science Center at Houston. Animals were fed a standard laboratory chow, LabDiet 5001 (PMI Nutrition International, St. Louis, MO, USA). C57BL/6J Mice were obtained from Jackson Laboratory (Bar Harbor, ME, USA; CAT#000664, RRID: IMSR_JAX:000664), and both male and female mice were used in experiments.

Cell lines, culture, and treatments.

L6 myoblasts (rat skeletal muscle cell line) were purchased from American Type Culture Collection (ATCC, Manassas, VA, USA; ATCC CAT#CRL-1458, RRID: CVCL_0385). L6Ms were grown in Dulbecco's Modified Eagle Medium (DMEM; Thermo Fisher Scientific, Hampton, NH, USA; CAT#10567022) supplemented with 10% (v/v) fetal bovine serum (FBS; Thermo Fisher Scientific, Hampton, NH, USA; CAT#16000044) and penicillin-streptomycin (100 units/mL; Thermo Fisher Scientific, Hampton, NH, USA; CAT#15140163) at 37°C and 5% CO_2 in a humidified incubator. Cultures were grown for at least five passages before differentiation or transfection. L6Ms fuse in culture to form multinucleated myotubes and striated fibers. For differentiation into myotubes, L6Ms were grown in DMEM supplemented with 1% (v/v) FBS for 72 h to promote cell differentiation and fusion. Cells were then maintained at 37°C and 5% CO_2 in a humidified incubator for the duration of the experiments, changing the media every 2-3 days. Differentiated L6Ms were treated for 24 h with phosphate-buffered saline (PBS, Sigma Aldrich, St. Louis, MO, USA; CAT#506552), D-2-hydroxyglutarate (D2-HG, 0 to 1.0 mmol/L; Tocris Bioscience, Minneapolis, MN, USA; CAT#6124), or dimethyl 2-oxoglutarate (DMKG, 1 mmol/L, Sigma Aldrich, St. Louis, MO, USA; CAT#349631).

Mitochondrial respirometry.

Oxygen consumption of intact L6Ms was measured using a Seahorse XF96 Extracellular Flux Analyzer. Cells were seeded at a density of 2 x 10^4 cells/well in a 96-well XF microplates cultured, and differentiated with DMEM (Thermo Fisher Scientific, Hampton, NH, USA; CAT#10567022) containing 10% (v/v) FBS (Thermo Fisher Scientific, Hampton, NH, USA;

CAT#16000044). One day before initiation of measurements, growth medium was replaced with XF-compatible DMEM (CAT#A14430-01, Thermo Fisher Scientific, Hampton, NH, USA) supplemented with physiologic concentrations of glucose (5.5 mmol/L; Sigma Aldrich, St. Louis, MO, USA; CAT#G8270), glutamine (0.5 mmol/L; Thermo Fisher Scientific, Hampton, NH, USA; CAT#25030081) and pyruvate (0.1 mmol/L; Thermo Fisher Scientific, Hampton, NH, USA; CAT#11360070). Cell were incubated at 37°C without CO_2 for 1 h to allow pre-equilibrate with the assay medium. oligomycin A (Sigma Aldrich, St. Louis, MO, USA; CAT#75351), Carbonyl cyanide 4-(trifluoromethoxy)phenylhydrazone (FCCP, Sigma Aldrich, St. Louis, MO, USA; CAT#C2920), rotenone/antimycin A (Sigma Aldrich, St. Louis, MO, USA; CAT#R8875 and CAT#A8674) were loaded into the Seahorse XF96 cartridge injector ports. The final concentrations for reagents were as follows: 1 μM oligomycin A, 8 μM FCCP, 0.5 μM rotenone/antimycin A. Oxygen consumption rate (OCR) and extracellular acidification rate (ECAR) were detected under basal conditions followed by sequential addition of oligomycin, FCCP, as well as rotenone/antimycin A. Measurements were analyzed using

Western blotting and Immunoprecipitation.

L6Ms were treated with PBS (control) or D2HG (0.5 mmol/L or 1 mmol/L) for 24 h. The activation of autophagy was assessed in cells using bafilomycin A1 (BafA1, 200 nmol/L; Sigma Aldrich, St. Louis, MO, USA, CAT#B1793). L6Ms were treated with BafA1 for 2 h before the end of the experimental protocol. Proteins were extracted from tissue and cell sample using RIPA lysis and extraction buffer (Thermo Fisher Scientific, Hampton, NH, USA, CAT#89900) per manufacturer's instructions. Tissue and cell homogenates for western blotting were prepared in the presence of phosphatase inhibitors (CAT#P5726 and CAT#P0044; Sigma-Aldrich, St. Louis, MO, USA) and protease inhibitors (cOmplete™ Protease Inhibitor Cocktail, Sigma-Aldrich, St. Louis, MO, USA; CAT#11697498001). Proteins were separated on 4-20% SDS-PAGE gels, transferred to PVDF membranes and probed with antibodies from Cell Signaling Technology (CS, Danvers, MA, USA) against LC3B (CS, CAT#3868), Sirt1 (CS, CAT#8469), SQSTM1/p62 (CS, CAT#23214), Acetylated-lysine antibody (CS, CAT#9441), p300 (CS, CAT#86377), GAPDH (CS, CAT#5174), normal rabbit IgG (CS, CAT#2729), AMPK (CS, CAT#5831), Phospho-AMPK (CS, CAT#50081), mTOR (CS, CAT#2972), Phospho-mTOR (CS, CAT#2971). Secondary antibodies conjugated to HRP were used following incubation with primary antibodies: anti-rabbit antibody (CS,

CAT#7074) and anti-mouse antibody (CS, CAT#7076). Levels of proteins were detected by immunoblotting using horseradish peroxidase-conjugated secondary antibodies and chemiluminescence. For immunoprecipitation experiments, cultured L6Ms were washed with ice-cold PBS twice and lysed in hypotonic/digitonin buffer containing 1,4-Piperazinediethanesulfonic acid (PIPES, 20 mmol/L, pH 7.2; Sigma-Aldrich, St. Louis, MO, USA; CAT#P6757), Ethylenedinitrilo)tetraacetic acid (EDTA, 5 mmol/L; Sigma-Aldrich, St. Louis, MO, USA; CAT#E9884), $MgCl_2$ (3 mmol/L; Sigma-Aldrich, St. Louis, MO, USA; CAT#M8266), glycerophosphate (10 mmol/L; Sigma-Aldrich, St. Louis, MO, USA; CAT#G9422), pyrophosphate (10 mmol/L; Sigma-Aldrich, St. Louis, MO, USA; CAT#P8010), digitonin (0.02%; Sigma-Aldrich, St. Louis, MO, USA; CAT#D141), as well as protease and phosphatase inhibitors (see above). After 40 min nutation at 4 ºC, samples were centrifuged at 20,000 x g for 7 min, and the supernatant transferred into new microcentrifuge tubes. LC3, Sirt1, or acetylated proteins were immunoprecipitated using the monoclonal antibody described above. Cell lysates were incubated (300 to 500 µg of total protein) with antibodies at 4ºC overnight. Immunocomplexes were then incubated for 2 h with protein A/G PLUS-agarose beads (30 µL of 50 % slurry; Thermo Fisher Scientific, Hampton, NH, USA; CAT#20423). Samples were washed with ice-cold lysis buffer four times, and beads were boiled in 4x Lithium dodecyl sulfate buffer (~30 µL; Thermo Fisher Scientific, Hampton, NH, USA; CAT#B0008) for 15 min at 37 ºC to elute captured protein. Samples were then subjected to Western blotting. Signals were quantified by densitometry using NIH ImageJ software (http://imagej.nih.gov/ij; Bethesda, MA, USA). Bands were normalized to that of loading control obtained from the same gel (GAPDH for whole cell lysate and target molecule of immunoprecipitation for the study of LC3 and Sirt1 interaction), and percentage of control was obtained.

Real Time-quantitative PCR (RT-qPCR).

RNA was extracted from L6Ms using the QIAGEN RNeasy Fibrous Tissue Mini Kit (Qiagen, Hilden, Germany; CAT#74704). RNA concentration was determined using a Qubit 4.0 fluorometer (Life Technologies) and Qubit™ RNA BR Assay Kit (ThermoFisher Scientific, Waltham, MA; CAT#Q10210) according to the manufacturer's instructions. The quality of each RNA sample was checked using an Agilent 4200 Tape Station with Agilent High Sensitivity RNA ScreenTape (Agilent Technologies, Santa Clara, CA, USA; CAT#5067-5579) according to

manufacturer's instructions. cDNAs were synthesized using the iScript gDNA Clear cDNA Synthesis Kit (Bio-Rad, Hercules, CA, USA; CAT#172-5035) from 500 ng of total RNAs. Quantitative PCRs were conducted by mixing cDNA samples (final concentration per well 10 ng) with iTaq Universal SYBR® Green Supermix (Bio-Rad, Hercules, CA, USA; CAT#172-5124) and the appropriate primers according to the manufacturer's instructions. The following validated primers from Bio-Rad (CAT#100-25636) were used in this study: Beclin1 (qRnoCID00038), Trim63 (qRnoCED0003), p62/Sqstm1 (qRnoCED0006), Microtubule-associated proteins 1A/1B light chain 3B (Map1/LC3B; qRnoCED0002031), atrogin-1 (MAFbx; qRnoCID0008629). Pre-designed primers for Peptidylprolyl isomerase A (cyclophilin A; Sigma-Aldrich; CAT#KSPQ12012,) were used for gene expression analysis. Quantitative PCR was conducted, including an RNA quality control (Bio-Rad, Hercules, CA, USA; CAT#10044157) and genomic DNA control (CAT#10044158, Bio-Rad, Hercules, CA, USA) for each sample. Real-Time PCR was conducted using a CFX384 Touch Real-Time PCR Detection System (Bio-Rad, Hercules, CA, USA). The cycling protocol was as follows: activation at 97°C for 2 min, followed by 40 cycles of denaturation at 95°C for 5 sec and annealing/extension at 60°C for 30 sec. At the end of the protocol, an additional Melt curve step was added at 65-95°C with 0.5°C increments for 5 sec/step.

Plasmid construction and L6M transfection.

Plasmid ptfLC3 (AddGene, Watertown, MA, USA; CAT#21074, RRID: Addgene_21074) was used to generate GFP-tagged LC3-K49R/K51R and LC3-K49Q/K51Q mutants. Site-directed mutagenesis was conducted using QuikChange Lightning site-directed mutagenesis kit (Agilent, Santa Clara, CA, USA; CAT#210515) according to the manufacturer's instructions and using the following primers: LC3-K49R/K51R-F (5'-GAACCTGGTCCTGTCCA -3') and LC3-K49R/K51R-R (5'-GTCCTGGACAGGACCA-3') and LC3-K49Q/K51Q-F (5'-GAACTGGGTCTGGTCCA-3') and LC3-K49Q/K51Q-R (5'- GGACCAGACCCAGTTCC-3'). Clones were confirmed by genomic DNA extraction using the QIAGEN Plasmid Maxi Kit (Qiagen, Hilden, Germany; CAT#12163), PCR amplification of the target loci with Q5® polymerase (New England Biolabs Inc., Ipswich, MA, USA; CAT#M0491S), and Sanger sequencing of PCR products (Genewiz LLC, South Plainfield, NJ, USA). L6Ms overexpressing p300 were generated using plasmid 1245 pCMVb p300 (AddGene, Watertown, MA, USA; CAT#10717, RRID: Addgene_10717). Transfections

were conducted using Lipofectamine™ 3000 (Invitrogen, Thermo Fisher Scientific, Hampton, NH, USA; CAT#L300008) according to the manufacturer's instructions. Briefly, L6Ms were grown to 70-80% confluence in a 6-well plate with DMEM containing 10% (v/v) FBS and penicillin-streptomycin (100 U/mL). Plasmid DNA-lipid complexes were in sterile OptiMEM (Gibco, Thermo Fisher Scientific, Hampton, NH, USA; CAT#51985091) by diluting DNA (0.1 μg/μL) and 5% Lipofectamine™ 3000 (v/v) separately. The diluted Lipofectamine™ was then added to the diluted DNA (1:1 ratio), mixed by gentle pipetting and incubated for 20 min at room temperature. The cell culture medium was removed from each well and replaced with a mix of serum-free DMEM and OptiMEM in a ratio of 1:0.8 (v/v) for the duration of the transfection. The DNA-lipid complexes were added to each well, and L6Ms were cultured for 18 h at 37°C and 5% CO_2. Then, the transfection medium was removed and replaced with 2 mL DMEM containing 10% FBS (v/v). After 24 h the cell culture medium was replaced with phenol red-free DMEM (Thermo Fisher Scientific, Hampton, NH, USA; CAT#11054020) containing 5 mmol/L glucose, 0.5 mmol/L glutamine and 0.5 mmol/L pyruvate. Negative controls for each experiment consisted of cultures treated with plasmid DNA or Lipofectamine™ only. For RNA interference (RNAi), Sirt1 siRNA (Sigma Aldrich, St Louis, MO, USA; CAT# NM_001107627) was used. Exponentially growing cells in a 6-well plate format were transfected with 100 μM of siRNA complex prepared in OptiMEM and transfected using Lipofectamine™ RNAiMAX (Invitrogen, Thermo Fisher Scientific, Hampton, NH, USA; CAT#13778075) according to manufacturer's instructions. Cells were incubated for an additional 72 h, and the silencing of proteins was confirmed by western blot. Following 48 h of Sirt1 silencing, cells were co-transfected with ptfLC3 plasmid and treated as described above.

Cell imaging and fluorescent puncta counting.

Cell treatments, microscopy, and puncta counting were conducted by six different researchers (two per task). L6Ms were imaged 24 h after treatments. Cell culture media was removed and replaced by fresh phenol red-free DMEM containing 5 mmol/L glucose, 0.5 mmol/L glutamine, and 0.5 mmol/L pyruvate. For lysosome imaging, L6Ms were live-stained with by adding 50 nmol/L Lysotracker-red DND-99 dye (Invitrogen, Waltham, MA, USA; CAT#L-7528) to the cell culture medium at 37°C for 30 min. Cells were then washed twice with Dulbeccos's phosphate-buffered saline (PBS; Gibco, Thermo Fisher Scientific, Hampton, NH, USA; CAT#14190-136)

and 2 mL of fresh phenol red-free DMEM containing 5 mmol/L glucose, 0.5 mmol/L glutamine and 0.5 mmol/L pyruvate was added. Image acquisition was carried out in an inverted Olympus IX81 microscope equipped with a ProScan II (Prior Scientific) motorized stage, a Lambda 10-3 filter wheel system, a Lumen 200 (Prior Scientific) fluorescence illumination system, a 60 x DIC objective, and a high-resolution Hamamatsu C10600 CCD camera. The GFP (Em = 472 ± 18 nm, Ex = 520 ± 18 nm) and TRITC (Em = 545 ± 20 nm, Ex = 593 ± 20 nm) filter sets were used to visualize LC3-GFP and Lysotracker-red staining, respectively. The exposure time was 2-5 s for LC3-GFP and 0.2-0.5 s for Lysotracker-red staining. All *in vitro* assays were conducted after treatments for 24 h with D2-HG. The image recordings were visualized and quantified in Fiji (Schindelin et al., 2012). Recordings allowed for counting of cells, and within those cells, the individual spots were counted manually by three independent users. Images were collected at similar magnification levels. The ratio of the total amount of spots over the total amount of cells was then calculated.

***In vivo* mouse strength testing.**

Male and female mice (10 weeks old) were treated with D2-HG for 30-days. During the time period, mice were subjected to weekly strength testing as described by Contet C. et al. (Contet et al., 2001). Briefly, grip strength was assessed using seven weights ranging from 20 g to 90 g (see **Figure 4A**). Each mouse was held by the middle/base of the tail and lowered to allow the mouse to grasp the first weight (20 g). Once the mouse grasped the weight-pouch with its forepaws, a stopwatch was started. Then, the mouse was raised until the pouch was clear of the table. Each weight had to be held by the animal for 3 seconds. Weights were tested sequentially, starting with the lowest at 20 g and up to 100 g. Between weights, mice were rested for about 10 sec. If a mouse failed to hold a weight, the mouse was rested for 10 sec and the same weight was tried again. The trial was terminated if a mouse failed to hold a weight three times. The final score was calculated as described by Deacon R.M.J. (Deacon, 2013).

Mouse tissue preparation and histology.

Mice were euthanized by chloralhydrate injection (500 mg/kg body weight), and tissue was dissected, fixed in 10% neutral-buffered formalin overnight, and dehydrated in 70% ethanol before paraffin embedding. Muscle cross-sections (5 μm) were cut and stained with hematoxylin

and eosin by the Histopathology Laboratory in the Department of Pathology and Laboratory Medicine within the McGovern Medical School at The University of Texas Health Science Center at Houston. Slides were imaged with a Keyence Microscope (Keyence, Itasca, IL, USA).

RNA sequencing.

RNA extraction and library preparation.

RNA-sequencing libraries were prepared using the Illumina TruSeq Stranded mRNA Sample Preparation Kit (Illumina, SanDiego, CA; CAT#20020594). RNA was extracted from 20 to 30 mg skeletal muscle tissue using the QIAGEN RNeasy Fibrous Tissue Mini Kit (Qiagen, Hilden, Germany; CAT#74704). RNA concentration was determined using a Qubit 4.0 fluorometer (Life Technologies) and Qubit™ RNA HS Assay Kit (Thermo Fisher Scientific, Waltham, MA; CAT#Q32852) according to the manufacturer's instructions. The quality of each RNA sample was checked using an Agilent 4200 Tape Station with Agilent High Sensitivity RNA ScreenTape (Agilent Technologies, Santa Clara, CA, USA; CAT#5067-5579) according to the manufacturer's instructions. For library preparation, poly-A RNA was purified from mRNA using oligo-dT magnetic beads. mRNA was fragmented, and cDNA synthesized. A-tailing was conducted to enable subsequent ligation of paired-end sequencing adapters. Library quality was determined using an Agilent 4200 Tape Station with Agilent High Sensitivity D5000 DNA ScreenTape (CAT#5067-5592, Agilent Technologies, Santa Clara, CA, USA) to ensure correct fragment sizes between 250 and 300 bp.

RNA sequencing and data processing.

Libraries were clustered onto a HiSeq patterned flow cell using a cBot2 system (Illumina, Inc., San Diego, CA, USA) and HiSeq 3000/4000 PE Cluster Kit (Illumina, Inc., San Diego, CA, USA; CAT#PE-410-1001). The clustered flow cell was then run on a HiSeq 4000 Sequencing System (Illumina, Inc., San Diego, CA, USA) using a HiSeq 3000/4000 SBS 300-cycle kit (Illumina, Inc., San Diego, CA, USA; CAT#FC-410-1003) for 2x150 paired-end reads. All instrument preparation and run parameters were carried out or selected according to manufacturer specifications. Raw reads from the sequencer were demultiplexed and converted to fastq format using bcl2fastq v2.19.1.403 (Illumina, Inc., San Diego, CA, USA), optioned to allow for 0 mismatch in the barcodes.

Targeted Metabolomics by Liquid Chromatography (LC) and Ion Chromatography (IC)-MS

The relative abundance of polar metabolites in mouse skeletal muscle (*M. gastrocnemius*) and L6 myocyte samples were analyzed from metabolite extracts by ultra-high-resolution mass spectrometry (HRMS). For tissue samples, approximately 10 to 20 mg of skeletal muscle were pulverized on liquid nitrogen then homogenized with Precellys Tissue Homogenizer (Bertin Instruments, Rockville, MD, USA; CAT#P000062-PEVO0-A). For cell samples, approximately 80% confluent cells were seeded in 10 cm dishes in triplicate. Metabolites were extracted using 1 mL ice-cold 0.1% Ammonium hydroxide in 80/20 (v/v) methanol/water. Extracts were centrifuged at 17,000 *g* for 5 min at 4°C, and supernatants were transferred to clean tubes, followed by evaporation to dryness under nitrogen. Dried extracts were reconstituted in deionized water prior to MS, and 5 µL were injected for analysis by ion chromatography (IC)-MS. IC mobile phase A (MPA; weak) was water, and mobile phase B (MPB; strong) was water containing 100 mM KOH. A Thermo Scientific Dionex ICS-5000+ system included a Thermo IonPac AS11 column (4 µm particle size, 250 x 2 mm) with a column compartment kept at 30°C. The autosampler tray was chilled to 4°C. The mobile phase flow rate was 360 µL/min, and the gradient elution program was: 0-5 min, 1% MPB; 5-25 min, 1-35% MPB; 25-39 min, 35-99% MPB; 39-49 min, 99% MPB; 49-50, 99-1% MPB. The total run time was 50 min. Methanol was delivered by an external pump and combined with the eluent via a low dead volume mixing tee to assist desolvation and increase sensitivity. Data were acquired using a Thermo Orbitrap Fusion Tribrid Mass Spectrometer under ESI negative ionization mode. For amino acid analysis, samples were diluted in 90/10 acetonitrile/water containing 1% formic acid, then 15 µL was injected for analysis by liquid chromatography (LC)-MS. LC mobile phase A (MPA; weak) was acetonitrile containing 1% formic acid, and mobile phase B (MPB; strong) was water containing 50 mM ammonium formate. A Thermo Vanquish LC system included an Imtakt Intrada Amino Acid column (3 µm particle size, 150 x 2.1 mm) with column compartment kept at 30°C. The autosampler tray was chilled to 4°C. The mobile phase flow rate was 300 µL/min, and the gradient elution program was: 0-5 min, 15% MPB; 5-20 min, 15-30% MPB; 20-30 min, 30-95% MPB; 30-40 min, 95% MPB; 40-41 min, 95-15% MPB; 41-50 min, 15% MPB. The total run time was 50 min. Data were acquired using a Thermo Orbitrap Fusion Tribrid Mass Spectrometer under ESI positive ionization mode at a resolution of 240,000. Raw data files were imported to TraceFinder™ 5.1 SP1 (Thermo Fisher Waltham, MA, USA; CAT#OPTON-31001) for peak

identification and quantification. Metabolites abundances were normalized by DNA concentrations.

Detection and quantification of D2-HG using LC-MS/MS.

After collection and washing, approximately 20,000 L6Ms were treated with 500 µl of cold 40% acetonitrile, 40% methanol, 20% water, vortexed vigorously for 15 min at 4 °C, and spun at 10,000 × *g* for 10 min at 4 °C. Supernatants were removed and dried to completion in a SpeedVac, and resuspended using 20 µl of methanol, followed by vortexing, and subsequently 80 µl of water was added along with a final vigorous vortexing. Standards of D2-HG sodium salt at 40mg/mL were prepared in water and serially diluted to generate a standard curve to assess linearity and for quantitation. Serially diluted samples were dried to completion in a SpeedVac and resuspended similarly to the samples as described above. Cell metabolite extractions were analyzed by injecting 4 µl of sample volume and using multiple reaction monitoring LC-MS with an Agilent 6470A triple quadrupole mass spectrometer. This instrument was operating in negative mode and connected to an Agilent 1290 ultra-high-performance liquid chromatography (UHPLC) system (Agilent Technologies, Santa Clara, CA). All mobile phase solvents consisted of HPLC or LC-MS grade reagents. Buffer A: water with 3% methanol, 10 mM tributylamine, and 15 mM glacial acetic acid. Buffers B: isopropyl alcohol. Buffer C: methanol with 10 nM tributylamine and 15 mM glacial acetic acid. Buffer D: acetonitrile. Finally, the analytical column used was an Agilent ZORBAX RRHD Extend-C18 1.8 µm 2.1 × 150 mm coupled with a ZORBAX Extend Fast Guard column for ultra-high-performance liquid chromatography Extend-C18, 2.1 mm, 1.8 µm. The resulting chromatograms were visualized in Agilent MassHunter Quantitative Analysis for QQQ (Agilent Technologies). According to our method and protocol, D2-HG eluted with a retention time of approximately 14 min and was identified by monitoring the transition of m/z 147.0 for precursor ion to m/z 129.1 and 101.2 for product ions. The final peak areas were manually checked for consistency and proper integration. Sample were normalized by DNA concentration.

Untargeted Proteomics by LC-MS/MS.

Tissue was fractionated into cytosolic-, myofilament-, and insoluble-enriched fractions by the “IN sequence” method as described previously (Kane et al., 2007). The skeletal muscle tissue was

cryo-homogenized at an approximate ratio of tissue weight to homogenization buffer volume at 1:4 (v/v). Tissue sample were separated into cytosolic-, myofilament-, and insoluble-enriched fractions using a homogenization buffer containing 250 mmol/L HEPES-NaOH (Sigma Aldrich, St. Louis, MO, USA; CAT#H3375), EDTA (2.5 mmol/L, pH 8.0; Sigma Aldrich, St. Louis, MO, USA; CAT#E9884), a homogenization buffer containing 1% trifluoroacetic acid (Sigma-Aldrich, St. Louis, MO, USA; CAT#299537), and a homogenization buffer containing 2% sodium dodecyl sulfate (SDS; Sigma Aldrich, St. Louis, MO, USA; CAT#L6026) respectively. Protein concentration was determined by Pierce™ BCA Protein Assay Kit (Thermo Fisher Scientific, Waltham, MA, USA; CAT#23225). Two hundred µg of each fraction (total protein quantification) were reduced using 1 mmol/L Tris(2-carboxyethyl)phosphine hydrochloride (TCEP, Sigma Aldrich, St. Louis, MO, USA; CAT#C4706). Samples were cleaned up and alkylated using filter-aided sample preparation (FASP 10 kDA). Samples were digested for 15–18h at 37°C using ultra-grade Trypsin (Promega, Madison, WI, USA; CAT#V5111) at a 1:100 enzyme: protein ratio. Samples were desalted using Oasis HLB 96-well plates (30 µm and 5 mg sorbent; Waters, Milford, MA, USA; CAT#18600309), vacuum-dried, and stored at –80°C until analysis.

For all methods, peptides were analyzed in two replicate runs by liquid chromatography-tandem mass spectrometry (LC-MS/MS) on a Dionex Ultimate 3000 NanoLC connected to an Orbitrap Fusion™ Lumos™ Tribrid™ Mass Spectrometer (ThermoFisher Scientific, Waltham, MA, USA) equipped with an EasySpray ion source as previously reported (Kooij et al., 2014).

(A) Analysis of nano-IP and gel pieces using short gradient

Lumos™, USAPeptides were loaded onto a PepMap RSLC C18 column (2 µm, 100 Å, 150 µm i.d. x 15 cm, ThermoFisher Scientific, Waltham, MA, USA) using a flow rate of 1.4 µL/min for 7 min at 1% B (mobile phase A was 0.1% formic acid in water and mobile phase B was 0.1 % formic acid in acetonitrile) after which point they were separated with a linear gradient of 5-35%B for 11 minutes, 35-85%B for 3 min, holding at 85%B for 5 minutes and re-equilibrating at 1%B for 17 minutes. The nano-source capillary temperature was set to 300°C and the spray voltage was set to 1.8 kV. MS1 scans were acquired in the Orbitrap at a resolution of 120,000 Hz in the mass range 400-1600 m/z. For MS1 scans the AGC (Automatic Gain Control) target was set to $4x10^5$ ions with a max fill time of 50 ms. MS2 spectra were acquired using the TopSpeed method

with a total cycle time of 3 seconds and an AGC target of $1x10^4$ and a max fill time of 100 ms, with an isolation width of 1.6 Da in the quadrupole. Precursor ions were fragmented using HCD (Higher-energy collisional dissociation) with a normalized collision energy of 30% and analyzed using rapid scan rates in the ion trap. Monoisotopic precursor selection was enabled, and only MS1 signals exceeding 5000 counts triggered the MS2 scans with +1 and unassigned charge states not being selected for MS2 analysis. Dynamic exclusion was enabled with a repeat count of 1 and exclusion duration of 15 seconds. Raw data was searched using the most recent version of the Uniprot rat database with the Sorcerer-Sequest™ search engine (Sagen-N Research Inc., Milpitas, CA, USA) with the following search parameters: full Trypsin cleavage, static modification of +57 Da on Cysteine, variable modification of +16 Da on Methionine (Oxidation), +54 Da on Arginine (Methylglyoxal-Hydroimidazolone 1, MG-H1), and +72 on Lysine (Carboxyethyl), with a MS1 error of 10 ppm, and MS2 error of 1 Da. Data was post processed using Scaffold 4 (www.proteomesoftware.com, Proteome Software, Inc., Portland, OR, USA).

(B) Discovery proteomic using long gradient.

Lumos™Peptides were loaded onto a PepMap RSLC C18 column (2 µm, 100 Å, 150 µm i.d. x 25 cm, ThermoFisher Scientific, Waltham, MA, USA) using a flow rate of 1.4 µL/min for 7 min at 1% B (mobile phase A was 0.1% formic acid in water and mobile phase B was 0.1 % formic acid in acetonitrile) after which point they were separated with a linear gradient of 5-20%B for 45 minutes, 20-35%B for 15 min, 35-85%B for 3 min, holding at 85%B for 5 minutes and re-equilibrating at 1%B for 5 minutes. Each sample was followed by a blank injection to both clean the column and re-equilibrate at 1%B. The nano-source capillary temperature was set to 300°C and the spray voltage was set to 1.8 kV. MS1 scans were acquired in the Orbitrap at a resolution of 240,000 Hz with the mass range 400-1600 m/z with advanced peak detection enabled. For MS1 scans the AGC target was set to $4x10^5$ ions with a max fill time of 50 ms. MS2 spectra were acquired using the TopSpeed method with a total cycle time of 3 seconds and an AGC target of $1x10^4$ and a max fill time of 50 ms, with an isolation width of 1.6 Da in the quadrapole. Precursor ions were fragmented using HCD with a normalized collision energy of 30% and analyzed using rapid scan rates in the ion trap. Monoisotopic precursor selection was enabled and only MS1 signals exceeding 5000 counts triggered the MS2 scans, with +1 and unassigned charge states not being selected for MS2 analysis. Dynamic exclusion was enabled with a repeat count of 1

and exclusion duration of 15 seconds. Raw data was searched using the most recent version of the Uniprot rat database with the Sorcerer-Sequest™ search engine (Sage-N Research Inc., Milpitas, CA, USA) with the following search parameters: full Trypsin cleavage, static modification of +57 Da on Cysteine, variable modification of +16 Da on Methionine (Oxidation), +54 Da on Arginine (Methylglyoxal-Hydroimidazolone 1, MG-H1), and +72 on Lysine (Carboxyethyl), with a MS1 error of 10 ppm, and MS2 error of 1 Da. Data was post processed using Scaffold 4 (www.proteomesoftware.com, Proteome Software, Inc., Portland, OR, USA).

Data processing for proteomics analysis.

Raw MS/MS data files were converted to mzXML format using MSconvert (v.3.0.6002) from ProteoWizard (Kessner et al., 2008) for peaklist generation and used for database searching using two engines, X! TANDEM Spectrum Modeler (v2013.06.15.1) (Craig and Beavis, 2004) and Comet (v2014.02 rev.2) (Eng et al., 2013). The dataset was searched against the concatenated target/decoy mouse UniProt Knowledgebase (34018 proteins and decoys, December 06, 2018) (Elias and Gygi, 2007); (Apweiler et al., 2004). The uniqueness of identified sequences assigned to non-reviewed proteins was validated by manual Blastp search, thus filtering multiple assigned peptides.

Protein isoforms were only reported if a peptide comprising an amino acid sequence that was unique to the isoform was identified. Protein quantification was carried out by averaging the raw peptide intensity among technical replicates and summed among cellular sub-fractions. The peptide signal intensity was normalized to the median of the overall sample signal intensity, and protein level abundance inference was calculated using the linear mixed effects model built into the open sources MSstats (v3.2.2) software suite (Choi et al., 2014).

QUANTIFICATION AND STATISTICAL ANALYSIS

Statistical analysis was conducted using RStudio Desktop (v1.2.5042 for Linux, Boston, MA, USA) (RStudio Team, 2020), Bioconductor (Gentleman et al., 2004; Huber et al., 2015), and GraphPad Prism (version 8.1.2 for MacOS, GraphPad Software, La Jolla California USA, www.graphpad.com). Indicated sample sizes (n) represent individual tissue samples. For GFP-puncta counting, sample size (n) represents the number of cells analyzed from three or more independent experiments. Sample size and power calculations for *in vitro* and *in vivo* were based

on Snedecor (Snedecor GW, 1989) and GPower (Faul, 2007) (version 3.1.9.2 for windows). The type 1 error and power were considered at 5% (*P-value* of 0.05) and 80%, respectively. The expected difference in the mean between groups was 50-30%, and the standard deviation of 25-12.5%.

Unsupervised hierarchical clustering.

Clustering was conducted using the R package 'pheatmap' (v1.0.12) after log2-transformation and z-score scaling of the data. The z-score is defined as follows:

$$Z = \frac{x - \mu}{\sigma}$$

where x denotes the observed value, μ the mean of the sample, and σ the standard deviation of the sample. The similarity between groups was assessed using an Euclidean distance, and the number of clusters was determined using the k-means algorithm. We applied the 'Elbow' method to determine the optimal numbers of clusters.

Linear models to identify multi-omics changes in response to D2-HG.

Linear models adjusted for sex and batch information were computed in R using the 'limma' package (v3.40.06). Linear models were applied to log2-transformed data. A comparison between groups was conducted by one-way ANOVA (two-sided) and Tukey's posthoc test to identify significance. Normality was tested using a Shapiro-Wilk test. *P*-values were corrected for multiple hypothesis using the Benjamini-Hochberg method, and samples with a false discovery rate (FDR) below 0.01 (RNA-sequencing), and 0.05 (proteomics and metabolomics) were considered statistically significant.

Pathway enrichment analysis.

We used the STRING database (Szklarczyk et al., 2019) to identify enriched pathways using differentially expressed genes and proteins from RNA-sequencing and MS-based proteomics, respectively. Significance of pathways was determined by the hypergeometric test (one-sided) in IPA and a permutation-based, non-parametric test in STRING. *P*-values were corrected for multiple hypotheses using the Benjamini-Hochberg methods, and pathways with FDR below 0.01 (RNA-sequencing), and 0.05 (proteins and metabolites) were considered significant.

Protein-Protein interaction (PPI) network analysis.

Functional interactions between proteins were determined using the STRING database (https://string-db.org) (Szklarczyk et al., 2019) and the STRING plugin tool for Cytoscape (v3.8.0) (Shannon et al., 2003) was used to visualize the PPI network. In the network, the nodes correspond to the proteins, and the edges represent the interactions.

Metabolite network generation.

Metabolite interaction networks were generated using the MetaMapp tool (http://metamapp.fiehnlab.ucdavis.edu) (Barupal et al., 2012). Metabolites from MS-based metabolomics data were annotated to PubChem CIDs, KEGG IDs, and SMILES codes. The pair-wise Tanimoto chemical similarity coefficients (Willett, 1998) were generated using the MetaMapp tool using a threshold of 0.7 (Barupal et al., 2012). Cytoscape was used to visualize the differential statistics output on network graphs. Statistical results (P-value <0.05) were mapped as color, and fold changes were mapped as node size.

Network generation from multi-omics data.

Differential expression analysis between groups was conducted using the linear models, as described above. Metabolites and proteins were mapped using UniProt Knowledgebase and KEGG IDs (Kanehisa, 2019; Kanehisa and Goto, 2000; Kanehisa et al., 2019). Pairwise Spearman's rank correlation and Pearson's correlation coefficient were calculated between metabolites and proteins using the R base function 'cor' and the network was plotted with Cytoscape (v3.8.0) (Shannon et al., 2003). In the network, each node represents a metabolite or protein, and an edge between two nodes represents a metabolite-metabolite, protein-protein, or metabolite-protein interaction. PPIs were determined using the STRING database (Szklarczyk et al., 2019).

REFERENCES

Amary, M.F., Bacsi, K., Maggiani, F., Damato, S., Halai, D., Berisha, F., Pollock, R., O'Donnell, P., Grigoriadis, A., Diss, T.*, et al.* (2011). IDH1 and IDH2 mutations are frequent events in central chondrosarcoma and central and periosteal chondromas but not in other mesenchymal tumours. J Pathol *224*, 334-343.

Anderson, L.J., Liu, H., and Garcia, J.M. (2017). Sex Differences in Muscle Wasting. Adv Exp Med Biol *1043*, 153-197.

Apweiler, R., Bairoch, A., Wu, C.H., Barker, W.C., Boeckmann, B., Ferro, S., Gasteiger, E., Huang, H., Lopez, R., Magrane, M.*, et al.* (2004). UniProt: the Universal Protein knowledgebase. Nucleic acids research *32*, D115-119.

Arya, R., Kedar, V., Hwang, J.R., McDonough, H., Li, H.H., Taylor, J., and Patterson, C. (2004). Muscle ring finger protein-1 inhibits PKC{epsilon} activation and prevents cardiomyocyte hypertrophy. J Cell Biol *167*, 1147-1159.

Barabutis, N., Dimitropoulou, C., Gregory, B., and Catravas, J.D. (2018). Wild-type p53 enhances endothelial barrier function by mediating RAC1 signalling and RhoA inhibition. J Cell Mol Med *22*, 1792-1804.

Baracco, E.E., Castoldi, F., Durand, S., Enot, D.P., Tadic, J., Kainz, K., Madeo, F., Chery, A., Izzo, V., Maiuri, M.C.*, et al.* (2019). alpha-Ketoglutarate inhibits autophagy. Aging (Albany NY) *11*, 3418-3431.

Barupal, D.K., Haldiya, P.K., Wohlgemuth, G., Kind, T., Kothari, S.L., Pinkerton, K.E., and Fiehn, O. (2012). MetaMapp: mapping and visualizing metabolomic data by integrating information from biochemical pathways and chemical and mass spectral similarity. BMC Bioinformatics *13*, 99.

Black, J.C., Mosley, A., Kitada, T., Washburn, M., and Carey, M. (2008). The SIRT2 deacetylase regulates autoacetylation of p300. Mol Cell *32*, 449-455.

Bodine, S.C., Latres, E., Baumhueter, S., Lai, V.K., Nunez, L., Clarke, B.A., Poueymirou, W.T., Panaro, F.J., Na, E., Dharmarajan, K.*, et al.* (2001). Identification of ubiquitin ligases required for skeletal muscle atrophy. Science *294*, 1704-1708.

Cancer Genome Atlas Research, N., Ley, T.J., Miller, C., Ding, L., Raphael, B.J., Mungall, A.J., Robertson, A., Hoadley, K., Triche, T.J., Jr., Laird, P.W.*, et al.* (2013). Genomic and epigenomic landscapes of adult de novo acute myeloid leukemia. N Engl J Med *368*, 2059-2074.

Choi, M., Chang, C.Y., Clough, T., Broudy, D., Killeen, T., MacLean, B., and Vitek, O. (2014). MSstats: an R package for statistical analysis of quantitative mass spectrometry-based proteomic experiments. Bioinformatics *30*, 2524-2526.

Contet, C., Rawlins, J.N., and Deacon, R.M. (2001). A comparison of 129S2/SvHsd and C57BL/6JOlaHsd mice on a test battery assessing sensorimotor, affective and cognitive behaviours: implications for the study of genetically modified mice. Behav Brain Res *124*, 33-46.

Cosper, P.F., and Leinwand, L.A. (2011). Cancer causes cardiac atrophy and autophagy in a sexually dimorphic manner. Cancer Res *71*, 1710-1720.

Cox, J., and Mann, M. (2012). 1D and 2D annotation enrichment: a statistical method integrating quantitative proteomics with complementary high-throughput data. BMC Bioinformatics *13 Suppl 16*, S12.

Craig, R., and Beavis, R.C. (2004). TANDEM: matching proteins with tandem mass spectra. Bioinformatics *20*, 1466-1467.

Deacon, R.M. (2013). Measuring the strength of mice. J Vis Exp.

DiNardo, C.D., Propert, K.J., Loren, A.W., Paietta, E., Sun, Z., Levine, R.L., Straley, K.S., Yen, K., Patel, J.P., Agresta, S.*, et al.* (2013). Serum 2-hydroxyglutarate levels predict isocitrate dehydrogenase mutations and clinical outcome in acute myeloid leukemia. Blood *121*, 4917-4924.

Elias, J.E., and Gygi, S.P. (2007). Target-decoy search strategy for increased confidence in large-scale protein identifications by mass spectrometry. Nature methods *4*, 207-214.

Eng, J.K., Jahan, T.A., and Hoopmann, M.R. (2013). Comet: an open-source MS/MS sequence database search tool. Proteomics *13*, 22-24.

Evans, W.J., Morley, J.E., Argiles, J., Bales, C., Baracos, V., Guttridge, D., Jatoi, A., Kalantar-Zadeh, K., Lochs, H., Mantovani, G.*, et al.* (2008). Cachexia: a new definition. Clin Nutr *27*, 793-799.

Faul, F., Erdfelder, E., Lang, A.-G., Buchner, A. (2007). G*Power 3: A flexible statistical power analysis program for the social, behavioral, and biomedical sciences. Behavior Research Methods *3*, 175-191.

Fearon, K., Strasser, F., Anker, S.D., Bosaeus, I., Bruera, E., Fainsinger, R.L., Jatoi, A., Loprinzi, C., MacDonald, N., Mantovani, G.*, et al.* (2011). Definition and classification of cancer cachexia: an international consensus. Lancet Oncol *12*, 489-495.

Friesen, D.E., Baracos, V.E., and Tuszynski, J.A. (2015). Modeling the energetic cost of cancer as a result of altered energy metabolism: implications for cachexia. Theor Biol Med Model *12*, 17.

Gallagher, I.J., Stephens, N.A., MacDonald, A.J., Skipworth, R.J., Husi, H., Greig, C.A., Ross, J.A., Timmons, J.A., and Fearon, K.C. (2012). Suppression of skeletal muscle turnover in cancer cachexia: evidence from the transcriptome in sequential human muscle biopsies. Clin Cancer Res *18*, 2817-2827.

Gentleman, R.C., Carey, V.J., Bates, D.M., Bolstad, B., Dettling, M., Dudoit, S., Ellis, B., Gautier, L., Ge, Y., Gentry, J.*, et al.* (2004). Bioconductor: open software development for computational biology and bioinformatics. Genome Biol *5*, R80.

Gomes, M.D., Lecker, S.H., Jagoe, R.T., Navon, A., and Goldberg, A.L. (2001). Atrogin-1, a muscle-specific F-box protein highly expressed during muscle atrophy. Proc Natl Acad Sci U S A *98*, 14440-14445.

Gonzalez-Rodriguez, A., Mayoral, R., Agra, N., Valdecantos, M.P., Pardo, V., Miquilena-Colina, M.E., Vargas-Castrillon, J., Lo Iacono, O., Corazzari, M., Fimia, G.M.*, et al.* (2014). Impaired autophagic flux is associated with increased endoplasmic reticulum stress during the development of NAFLD. Cell Death Dis *5*, e1179.

Han, Y., Jin, Y.H., Kim, Y.J., Kang, B.Y., Choi, H.J., Kim, D.W., Yeo, C.Y., and Lee, K.Y. (2008). Acetylation of Sirt2 by p300 attenuates its deacetylase activity. Biochem Biophys Res Commun *375*, 576-580.

Hariharan, N., Maejima, Y., Nakae, J., Paik, J., Depinho, R.A., and Sadoshima, J. (2010). Deacetylation of FoxO by Sirt1 Plays an Essential Role in Mediating Starvation-Induced Autophagy in Cardiac Myocytes. Circ Res *107*, 1470-1482.

Huang, R., Xu, Y., Wan, W., Shou, X., Qian, J., You, Z., Liu, B., Chang, C., Zhou, T., Lippincott-Schwartz, J.*, et al.* (2015). Deacetylation of nuclear LC3 drives autophagy initiation under starvation. Mol Cell *57*, 456-466.

Huber, W., Carey, V.J., Gentleman, R., Anders, S., Carlson, M., Carvalho, B.S., Bravo, H.C., Davis, S., Gatto, L., Girke, T.*, et al.* (2015). Orchestrating high-throughput genomic analysis with Bioconductor. Nat Methods *12*, 115-121.

Intlekofer, A.M., Dematteo, R.G., Venneti, S., Finley, L.W., Lu, C., Judkins, A.R., Rustenburg, A.S., Grinaway, P.B., Chodera, J.D., Cross, J.R.*, et al.* (2015). Hypoxia Induces Production of L-2-Hydroxyglutarate. Cell Metab *22*, 304-311.

Intlekofer, A.M., Wang, B., Liu, H., Shah, H., Carmona-Fontaine, C., Rustenburg, A.S., Salah, S., Gunner, M.R., Chodera, J.D., Cross, J.R.*, et al.* (2017). L-2-Hydroxyglutarate production arises from noncanonical enzyme function at acidic pH. Nat Chem Biol *13*, 494-500.

Jassal, B., Matthews, L., Viteri, G., Gong, C., Lorente, P., Fabregat, A., Sidiropoulos, K., Cook, J., Gillespie, M., Haw, R.*, et al.* (2020). The reactome pathway knowledgebase. Nucleic Acids Res *48*, D498-D503.

Kane, L.A., Neverova, I., and Van Eyk, J.E. (2007). Subfractionation of heart tissue: the "in sequence" myofilament protein extraction of myocardial tissue. Methods Mol Biol *357*, 87-90.

Kanehisa, M. (2019). Toward understanding the origin and evolution of cellular organisms. Protein Sci *28*, 1947-1951.

Kanehisa, M., and Goto, S. (2000). KEGG: kyoto encyclopedia of genes and genomes. Nucleic Acids Res *28*, 27-30.

Kanehisa, M., Sato, Y., Furumichi, M., Morishima, K., and Tanabe, M. (2019). New approach for understanding genome variations in KEGG. Nucleic Acids Res *47*, D590-D595.

Karlstaedt, A., Zhang, X., Vitrac, H., Harmancey, R., Vasquez, H., Wang, J.H., Goodell, M.A., and Taegtmeyer, H. (2016). Oncometabolite d-2-hydroxyglutarate impairs alpha-ketoglutarate dehydrogenase and contractile function in rodent heart. Proc Natl Acad Sci U S A *113*, 10436-10441.

Kessner, D., Chambers, M., Burke, R., Agus, D., and Mallick, P. (2008). ProteoWizard: open source software for rapid proteomics tools development. Bioinformatics *24*, 2534-2536.

Kir, S., and Spiegelman, B.M. (2016). Cachexia & Brown Fat: A Burning Issue in Cancer. Trends Cancer *2*, 461-463.

Klionsky, D.J., Abdelmohsen, K., Abe, A., Abedin, M.J., Abeliovich, H., Acevedo Arozena, A., Adachi, H., Adams, C.M., Adams, P.D., Adeli, K.*, et al.* (2016). Guidelines for the use and interpretation of assays for monitoring autophagy (3rd edition). Autophagy *12*, 1-222.

Kooij, V., Venkatraman, V., Kirk, J.A., Ubaida-Mohien, C., Graham, D.R., Faber, M.J., and Van Eyk, J.E. (2014). Identification of cardiac myofilament protein isoforms using multiple mass spectrometry based approaches. Proteomics Clinical applications *8*, 578-589.

Kranendijk, M., Struys, E.A., Gibson, K.M., Wickenhagen, W.V., Abdenur, J.E., Buechner, J., Christensen, E., de Kremer, R.D., Errami, A., Gissen, P.*, et al.* (2010a). Evidence for genetic heterogeneity in D-2-hydroxyglutaric aciduria. Hum Mutat *31*, 279-283.

Kranendijk, M., Struys, E.A., Salomons, G.S., Van der Knaap, M.S., and Jakobs, C. (2012). Progress in understanding 2-hydroxyglutaric acidurias. J Inherit Metab Dis *35*, 571-587.

Kranendijk, M., Struys, E.A., van Schaftingen, E., Gibson, K.M., Kanhai, W.A., van der Knaap, M.S., Amiel, J., Buist, N.R., Das, A.M., de Klerk, J.B.*, et al.* (2010b). IDH2 mutations in patients with D-2-hydroxyglutaric aciduria. Science *330*, 336.

Lee, I.H., and Finkel, T. (2009). Regulation of autophagy by the p300 acetyltransferase. J Biol Chem *284*, 6322-6328.

Lok, C. (2015). Cachexia: The last illness. Nature *528*, 182-183.

Louis, D.N., Perry, A., Reifenberger, G., von Deimling, A., Figarella-Branger, D., Cavenee, W.K., Ohgaki, H., Wiestler, O.D., Kleihues, P., and Ellison, D.W. (2016). The 2016 World Health Organization Classification of Tumors of the Central Nervous System: a summary. Acta Neuropathol *131*, 803-820.

Lu, C., Venneti, S., Akalin, A., Fang, F., Ward, P.S., Dematteo, R.G., Intlekofer, A.M., Chen, C., Ye, J., Hameed, M.*, et al.* (2013). Induction of sarcomas by mutant IDH2. Genes Dev *27*, 1986-1998.

Marino, G., Pietrocola, F., Eisenberg, T., Kong, Y., Malik, S.A., Andryushkova, A., Schroeder, S., Pendl, T., Harger, A., Niso-Santano, M.*, et al.* (2014a). Regulation of autophagy by cytosolic acetyl-coenzyme A. Mol Cell *53*, 710-725.

Marino, G., Pietrocola, F., Kong, Y., Eisenberg, T., Hill, J.A., Madeo, F., and Kroemer, G. (2014b). Dimethyl alpha-ketoglutarate inhibits maladaptive autophagy in pressure overload-induced cardiomyopathy. Autophagy *10*, 930-932.

Miller, A.M., Shah, R.H., Pentsova, E.I., Pourmaleki, M., Briggs, S., Distefano, N., Zheng, Y., Skakodub, A., Mehta, S.A., Campos, C.*, et al.* (2019). Tracking tumour evolution in glioma through liquid biopsies of cerebrospinal fluid. Nature *565*, 654-658.

Miller, L.R., Marks, C., Becker, J.B., Hurn, P.D., Chen, W.J., Woodruff, T., McCarthy, M.M., Sohrabji, F., Schiebinger, L., Wetherington, C.L.*, et al.* (2017). Considering sex as a biological variable in preclinical research. FASEB J *31*, 29-34.

Montalvo, R.N., Counts, B.R., and Carson, J.A. (2018). Understanding sex differences in the regulation of cancer-induced muscle wasting. Curr Opin Support Palliat Care *12*, 394-403.

Moore, T.M., Zhou, Z., Cohn, W., Norheim, F., Lin, A.J., Kalajian, N., Strumwasser, A.R., Cory, K., Whitney, K., Ho, T.*, et al.* (2019). The impact of exercise on mitochondrial dynamics and the role of Drp1 in exercise performance and training adaptations in skeletal muscle. Mol Metab *21*, 51-67.

Nadtochiy, S.M., Urciuoli, W., Zhang, J., Schafer, X., Munger, J., and Brookes, P.S. (2015). Metabolomic profiling of the heart during acute ischemic preconditioning reveals a role for SIRT1 in rapid cardioprotective metabolic adaptation. J Mol Cell Cardiol *88*, 64-72.

Oberg, A.I., Dehvari, N., and Bengtsson, T. (2011). beta-Adrenergic inhibition of contractility in L6 skeletal muscle cells. PLoS One *6*, e22304.

Ogawa, M., Kitakaze, T., Harada, N., and Yamaji, R. (2015). Female-specific regulation of skeletal muscle mass by USP19 in young mice. J Endocrinol *225*, 135-145.

Pan, B., Li, J., Parajuli, N., Tian, Z., Wu, P., Lewno, M.T., Zou, J., Wang, W., Bedford, L., Mayer, R.J.*, et al.* (2020). The Calcineurin-TFEB-p62 Pathway Mediates the Activation of Cardiac Macroautophagy by Proteasomal Malfunction. Circ Res *127*, 502-518.

Pansuriya, T.C., van Eijk, R., d'Adamo, P., van Ruler, M.A., Kuijjer, M.L., Oosting, J., Cleton-Jansen, A.M., van Oosterwijk, J.G., Verbeke, S.L., Meijer, D.*, et al.* (2011). Somatic mosaic IDH1 and IDH2 mutations are associated with enchondroma and spindle cell hemangioma in Ollier disease and Maffucci syndrome. Nat Genet *43*, 1256-1261.

RStudio Team (2020). RStudio: Integrated Development for R. (RStudio, PBC, Boston, MA).

Runwal, G., Stamatakou, E., Siddiqi, F.H., Puri, C., Zhu, Y., and Rubinsztein, D.C. (2019). LC3-positive structures are prominent in autophagy-deficient cells. Sci Rep *9*, 10147.

Salazar-Degracia, A., Granado-Martinez, P., Millan-Sanchez, A., Tang, J., Pons-Carreto, A., and Barreiro, E. (2019). Reduced lung cancer burden by selective immunomodulators elicits improvements in muscle proteolysis and strength in cachectic mice. J Cell Physiol *234*, 18041-18052.

Schindelin, J., Arganda-Carreras, I., Frise, E., Kaynig, V., Longair, M., Pietzsch, T., Preibisch, S., Rueden, C., Saalfeld, S., Schmid, B.*, et al.* (2012). Fiji: an open-source platform for biological-image analysis. Nat Methods *9*, 676-682.

Shah, A., Diculescu, V.C., Qureshi, R., and Oliveira-Brett, A.M. (2010). Electrochemical reduction mechanism of camptothecin at glassy carbon electrode. Bioelectrochemistry *79*, 173-178.

Shannon, P., Markiel, A., Ozier, O., Baliga, N.S., Wang, J.T., Ramage, D., Amin, N., Schwikowski, B., and Ideker, T. (2003). Cytoscape: a software environment for integrated models of biomolecular interaction networks. Genome Res *13*, 2498-2504.

Shen, Q., Shi, Y., Liu, J., Su, H., Huang, J., Zhang, Y., Peng, C., Zhou, T., Sun, Q., Wan, W.*, et al.* (2020). Acetylation of STX17 (syntaxin 17) controls autophagosome maturation. Autophagy, 1-13.

Shimizu, K., Quillinan, N., Orfila, J.E., and Herson, P.S. (2016). Sirtuin-2 mediates male specific neuronal injury following experimental cardiac arrest through activation of TRPM2 ion channels. Exp Neurol *275 Pt 1*, 78-83.

Smith, K.L., and Tisdale, M.J. (1993). Increased protein degradation and decreased protein synthesis in skeletal muscle during cancer cachexia. Br J Cancer *67*, 680-685.

Snedecor GW, C.W. (1989). Statistical methods, 8 edn (Iowa State University Press).

Spangenburg, E.E., Geiger, P.C., Leinwand, L.A., and Lowe, D.A. (2012). Regulation of physiological and metabolic function of muscle by female sex steroids. Med Sci Sports Exerc *44*, 1653-1662.

Sylow, L., Jensen, T.E., Kleinert, M., Mouatt, J.R., Maarbjerg, S.J., Jeppesen, J., Prats, C., Chiu, T.T., Boguslavsky, S., Klip, A.*, et al.* (2013). Rac1 is a novel regulator of contraction-stimulated glucose uptake in skeletal muscle. Diabetes *62*, 1139-1151.

Szklarczyk, D., Gable, A.L., Lyon, D., Junge, A., Wyder, S., Huerta-Cepas, J., Simonovic, M., Doncheva, N.T., Morris, J.H., Bork, P.*, et al.* (2019). STRING v11: protein-protein association networks with increased coverage, supporting functional discovery in genome-wide experimental datasets. Nucleic Acids Res *47*, D607-D613.

VanderVeen, B.N., Fix, D.K., and Carson, J.A. (2017). Disrupted Skeletal Muscle Mitochondrial Dynamics, Mitophagy, and Biogenesis during Cancer Cachexia: A Role for Inflammation. Oxid Med Cell Longev *2017*, 3292087.

Vasyutina, E., Martarelli, B., Brakebusch, C., Wende, H., and Birchmeier, C. (2009). The small G-proteins Rac1 and Cdc42 are essential for myoblast fusion in the mouse. Proc Natl Acad Sci U S A *106*, 8935-8940.

Willett, P.B., J.M.; Downs, G.M. (1998). Chemical similarity searching. J Chem Inf Comput Sci *38*, 983-996.

Yamamoto, A., Tagawa, Y., Yoshimori, T., Moriyama, Y., Masaki, R., and Tashiro, Y. (1998). Bafilomycin A1 prevents maturation of autophagic vacuoles by inhibiting fusion between autophagosomes and lysosomes in rat hepatoma cell line, H-4-II-E cells. Cell Struct Funct *23*, 33-42.

Yi, C., Ma, M., Ran, L., Zheng, J., Tong, J., Zhu, J., Ma, C., Sun, Y., Zhang, S., Feng, W.*, et al.* (2012). Function and molecular mechanism of acetylation in autophagy regulation. Science *336*, 474-477.

Yoon, S.L., Grundmann, O., Williams, J.J., Gordan, L., and George, T.J., Jr. (2018). Body composition changes differ by gender in stomach, colorectal, and biliary cancer patients with cachexia: Results from a pilot study. Cancer Med *7*, 3695-3703.

Zhao, S., Torres, A., Henry, R.A., Trefely, S., Wallace, M., Lee, J.V., Carrer, A., Sengupta, A., Campbell, S.L., Kuo, Y.M.*, et al.* (2016). ATP-Citrate Lyase Controls a Glucose-to-Acetate Metabolic Switch. Cell Rep *17*, 1037-1052.